A finite element approach to model high-velocity impact on thin woven GFRP plates

A finite element approach to model high-velocity impact on thin woven GFRP plates

L. Alonso[a,b], F. Martínez-Hergueta[c], D. Garcia-Gonzalez[b], C. Navarro[b], S.K. García-Castillo[b], F. Teixeira-Dias[c]

[a]*Department of Chemical Technology, Energy and Mechanics, Rey Juan Carlos University C/Tulipán s.n., 28933*
[b]*Department of Continuum Mechanics and Structural Analysis, University Carlos III of Madrid Avda. de la Universidad 30, 28911*
[c]*School of Engineering, IIE — Institute for Infrastructure and Environment, The University of Edinburgh Edinburgh EH9 3JL, UK*

Abstract

A finite element model to predict the ballistic behaviour of woven GFRP laminates is presented. This finite element model incorporates a new constitutive model based on a continuum damage mechanics approach able to predict the performance of these laminates under high-velocity impacts. The material parameters of the model are identified from the literature and original experiments conducted in this work. The predictive capability of the model is verified against experimental impact tests. Finally, the model is used to analyse the influence of laminate thickness on different energy absorption mechanisms at velocities near the ballistic limit. This analysis allows for the determination of the principal deformation and failure mechanisms governing the perforation process.

Keywords: Laminate, Impact behaviour, Numerical modelling, High-velocity impact

1. Introduction

Composite materials are widely used for structural applications in different industrial sectors such as aerospace or naval. In particular, plain woven glass-fibre laminates are commonly used in the maritime and ground-transport industries, as well as in civil infrastructures due to their light weight, high stiffness and strength (Walter et al. (2009)). Since the use of composite materials is still increasing and these structures may be subjected to impacts during their service life, the experimental, numerical and analytical study of this phenomenon is a hot topic and is in continuous development (Fatt and Lin (2004)). Regarding numerical models, different approaches based on the finite element method (FEM) have been used to successfully simulate laminate penetration mechanics for quasi-static shear punch tests, low and high velocity ballistic impact (Xiao et al. (2007), Silva et al. (2005), Gower et al. (2008), García-Castillo et al. (2013), Chu et al. (2016), Briesciani et al. (2016), Ansari et al. (2017)). Depending on the failure mechanisms that need to be captured, numerical models can be two- or three-dimensional.

On the one hand, several models to predict intralaminar failure modes can be found in the literature. Among these 2D models for impact, Iannucci et al. (2001) proposed a progressive damage model based on an energy dissipation approach for woven glass-fibre composites. This model was validated with beam impact experiments and takes into account strain rate effects to predict fibre fracture and matrix cracking in the in-plane directions. Davila et al. (2005) proposed the LaRC04 2D model for unidirectional (UD) materials, based on phenomenological functions whose parameters are determined from specific experimental data, improving on Hashin's criteria (Hashin (1980)). The main novelty of this model is the better agreement with the experimental results in terms of failure mechanisms such as matrix and fibre failure in compression. In addition, the curve-fitting parameters are reduced in this model. Following the same trend, Miamí et al. (2007a) and Miamí et al. (2007b) developed a constitutive model valid to predict the onset and growth of

intralaminar failure mechanisms in composite laminates. The model is based on four possible fracture planes using a simplification of LaRC04 failure criteria, which is fully explained by Davila et al. (2005). 2D models can provide particularly good and efficient predictions for low-velocity impact for laminate thicknesses low enough to neglect the out-of-plane effects. Conversely, such 2D models are limited when dealing with thick specimens, as out-of-plane effects are not considered. For instance, some of these approaches (Iannucci et al. (2001)) neglect normal stresses across the thickness and may introduce relevant inaccuracies at high-velocity impacts on thick laminates.

On the other hand, most of the current 3D models to tackle impact simulations consider both in-plane and out-of-plane effects. Iannucci and Willows (2005) developed a 3D model to predict the impact response of woven composite materials. This model considers four damage variables that account for fibre failure in tension and compression (in-plane) and an additional one to take into account the interply failure associated to delamination. The evolution of damage is formulated in such a way as to allow control of the energy dissipated by each failure mode. Silva et al. (2005) used a 3D damage model in which parameters such as the Poisson's ratios or a parameter to take into account the residual shear stiffness had to be obtained by calibration with finite element models and experiments, respectively. Gower et al. (2008) also used numerical simulations to calibrate properties such as the out-of-plane failure shear stresses. García-Castillo et al. (2013) carried out finite element simulations in GFRP laminates applying a modification of Hou's criteria. These criteria consider failure of fibres in tension and compression (in-plane) and the transverse loads are assumed to be supported by the matrix, inducing delamination with a fifth damage variable. Briesciani et al. (2016) analysed the impact behaviour of tungsten blunt projectiles on fabric reinforced composites made of kevlar 29 plain-woven fabrics with an epoxy matrix using two different approaches, a macro-homogeneous model and a meso-heterogeneous model. In the former, matrix failure under tension and compression is formulated by means of the Tsai-Wu criterion in LS-DYNA. The out-of-plane effects are incorporated by means of a variable associated to delamination. Ansari et al. (2017) proposed a continuum damage formulation to take into account both in-plane and out-of-plane failure modes, modifying Hashin's failure criteria. Delamination is accounted for by means of a material parameter that degrades the shear stiffness. This model was used to predict the ballistic performance of GFRP plates against conical-nosed steel projectiles. Other 3D models are also used to simulate tests in quasi-static conditions instead of impacts tests such as the one used by Xiao et al. (2007) who considered an anisotropic damage mechanics approach defining different failure modes.

From the analysis of the above models, a clear division of failure criteria is observed into in-plane and out-of-plane mechanisms. The latter is more relevant when the thickness is large enough to enhance effects such as out-of-plane compression and out-of-plane shear stresses. The composite modelling can be accomplished by means of macro-, meso- or micro-mechanical approaches depending on the definition of the constituents as well as the spatial discretisation. The common point of these models is, however, the high number of fitting parameters that complicate the calibration of the models (Silva et al. (2005), Gower et al. (2008)). Moreover, most of the models associate the out-of-plane failure variable to delamination. Therefore, there is not a clear equivalence between the failure modes and the out-of-plane energy absorption mechanisms that can be found in the classic analytical models (Moyre et al. (2000), Naik and Doshi (2005), Alonso et al. (2018a)).

To overcome this limitation when combining analytical and numerical models to characterise the ballistic response of thin woven GFRP laminates, this work provides a new continuum damage model based on energy absorption mechanisms. To this end, a formulation is developed to simulate the phenomenon of damage in woven glass-fibre composites under out-of-plane dynamic loads. The constitutive response of the material is defined on the basis of a new macro-mechanical continuum damaged model. This damaged model accounts for the different failure mechanisms described in the theoretical model proposed by Alonso et al. (2018a). To do so, each failure mechanism is associated to an energy absorption mechanism in the theoretical model to provide a physical interpretation and capture all the relevant failure mechanisms. This model differentiates between shear plugging, compression out-of-plane failure mechanisms along with delamination, which is a more clear and accurate description.

The model is implemented in an explicit FEM framework for Abaqus/Explicit by a VUMAT user-subroutine. Furthermore, in order to capture interply damage, a cohesive damage model is included to account for delamination. Finally, a rate dependent friction model is implemented instead of the classic

Coulomb model. The influence of the laminate thickness on the activation and relevance of the different energy absorption mechanisms is studied. This analysis provides new insights into the coupling of energy absorption/failure mechanisms during the perforation process.

2. Experimental procedure

2.1. Material description

Woven E-glass/polyester laminates were tested in this work, which were previously characterised by García-Castillo et al. (2006), Buitrago-Pérez et al. (2010) and Alonso et al. (2018a). The woven laminates were manufactured by the staking of laminae embedded in a polyester matrix. Each 0.6 mm thick lamina consists of perpendicularly interlaced fibres that are parallel with the laminate border forming a woven alignment with a stacking sequence of $[0/90]_{ns}$ for 3 mm and 6 mm. The number of fibres is the same in both in-plane perpendicular directions. Important characteristics of this material include its high resistance given by E-glass fibres and the high deformations that the laminates can resist under high-velocity impact. The static properties obtained in previous works are listed in Table 1. There were, however, properties for the numerical model that needed to be obtained or estimated, such as the shear moduli (directions 13 and 23) and the failure stresses. The experimental procedure to obtain such properties is presented in the following sections, together with the results obtained. The dynamic properties at high strain rates used in the numerical model are estimated from the static properties obtained in the tests taking into account the relations proposed by Harding and Welsh (1983) and Harding and Ruiz (1998). The high-strain rate correction factors for the failure limits and for the shear and Young's moduli are estimated at 1.5 and 3 respectively. As assumed in other recent works (Corigliano et al. (2000); Dayou et al. (2019)), a single value of the Poisson's ratio has been used for all material directions.

Table 1: Summary of the static properties of woven E-glass fibre/polyester laminates.

Property	**Nomenclature**	**Quasi-static Value**	**Dynamic Value**
Laminate density [kg/m^3]	ρ_l	1980	1980
Young's modulus in directions 11 and 22 [GPa]	$E_{11} = E_{22}$	10.1	15.2
Young's modulus in direction 33 [GPa]	E_{33}	4.5	6.75
Shear modulus in direction 12 [GPa]	G_{12}	4.4	6.5
Poisson's coefficient	$\nu_{12} = \nu_{23} = \nu_{31}$	0.16	0.16
Failure stress in directions 11 and 22 [MPa]	$X_{11_t} = X_{22_t}$	367	1102
Failure stress in direction 33 [MPa]	X_{33_c}	464	1392
Failure shear stress in directions 12, 23 and 13 [MPa]	$S_{12} = S_{23} = S_{13}$	136	204

2.2. Shear tests

The shear moduli in directions 13 and 23, since the laminates are orthotropic, were determined from shear tests carried out by Alonso et al. (2018a). As the test configuration is similar to what happens during an impact, it is reasonable to calculate the shear moduli in this study. With the experimental set-up described by Alonso et al. (2018a) G_{13} and G_{23} can be approximated with the following expressions:

$$\gamma_{13} = \frac{x}{r} \tag{1}$$

$$G_{13} = G_{23} = \frac{F}{A_T \gamma_{13}} = \frac{F}{2\pi r e \gamma_{13}} \tag{2}$$

where γ_{13} is an estimated angular strain, A_T is the affected transverse area and F is the load. These magnitudes, together with the dimensions x and r, are shown in Fig. 1. Two tests were carried out and the mean curve is shown in Fig. 2.

From the results in Fig. 2, G_{13} can be obtained. As a first approach, we consider an idealised linear-elastic behaviour until failure. To this end, a representative curve can be determined from the mean σ_{13} vs

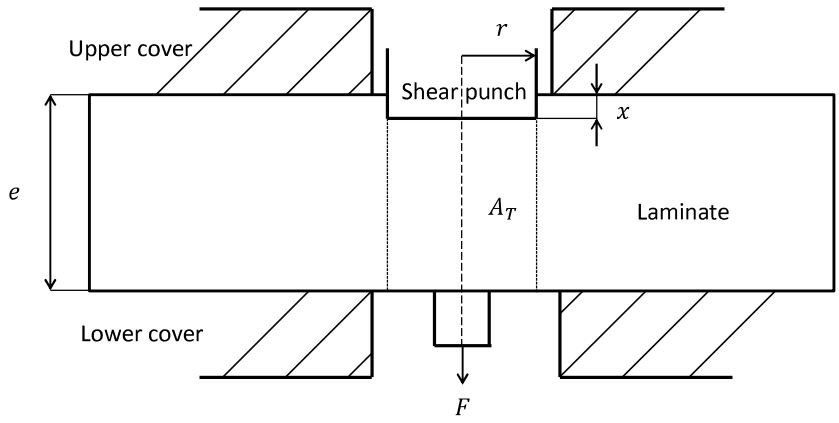

Figure 1: Shear test configuration.

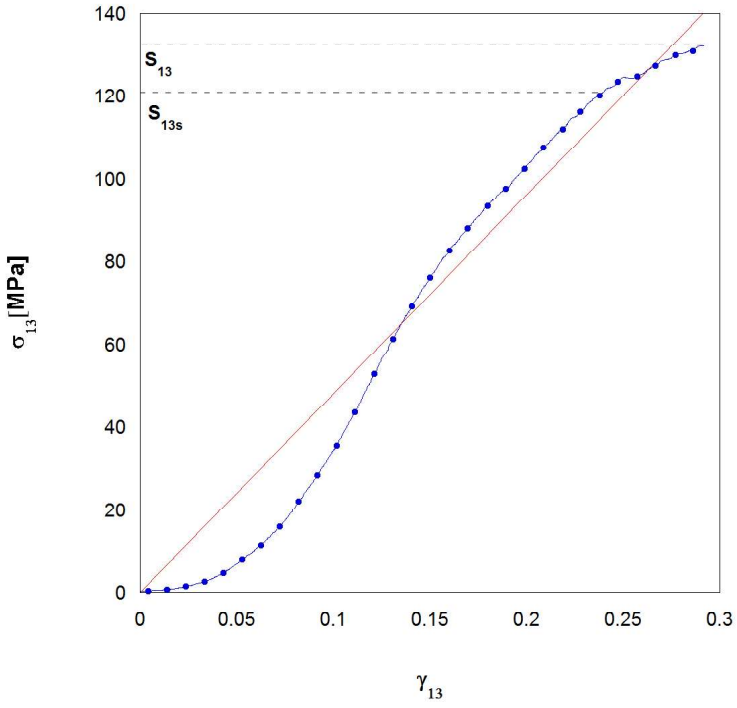

Figure 2: Mean σ_{13} vs γ_{13} curve for the shear tests performed at a velocity of 1 mm/min.

γ_{13} curve (original experimental data). This can be improved in future models to consider the non-linear behaviour of the material in 13 and 23 shear directions.

An additional hypothesis is that shear fibre failure strength S_{13} is different from the shear failure matrix strength S_{13s}. Furthermore, S_{13s} is lower than S_{13} because it is considered that the failure of the matrix takes place before the failure of the fibres in shear directions. This approach was used by other authors Xiao et al. (2007) and it can be backed up experimentally as shown in Figure 2, for directions 13 and 23. The methodology to compute the ultimate shear strengths for direction 12 is the same than for directions 13 and 23. We can observe in Fig. 2 that, from approximately 0.12 GPa, the curve becomes unstable and oscillations appear before complete failure. This point is associated with matrix shear failure and the maximum value with shear fibre failure stress.

2.3. In-plane compression tests

In-plane compression tests were carried out with the aim of characterising the compressive failure stress in directions 11 and 22. The standard test to measure compressive properties of composite materials is ASTM-Standard-D3410/D-3410M-95 (2010), which specifies that specimens should be rectangles 25×140 [mm^2]. The thickness of the specimens was 3 mm and the gap chosen for the tests was 10 mm. In order to carry out the experiments, an Instron 8802 universal test machine was used together with rosettes to measure the strain along the load direction as well as the perpendicular direction to check for bucking effects. The force and the longitudinal displacement were recorded and the stress-strain curve is shown in Figure 3. These results show the almost perfect linear-elastic response of the laminate under in-plane compression in direction 11. From this data, the compressive failure stress in direction 11 can be determined.

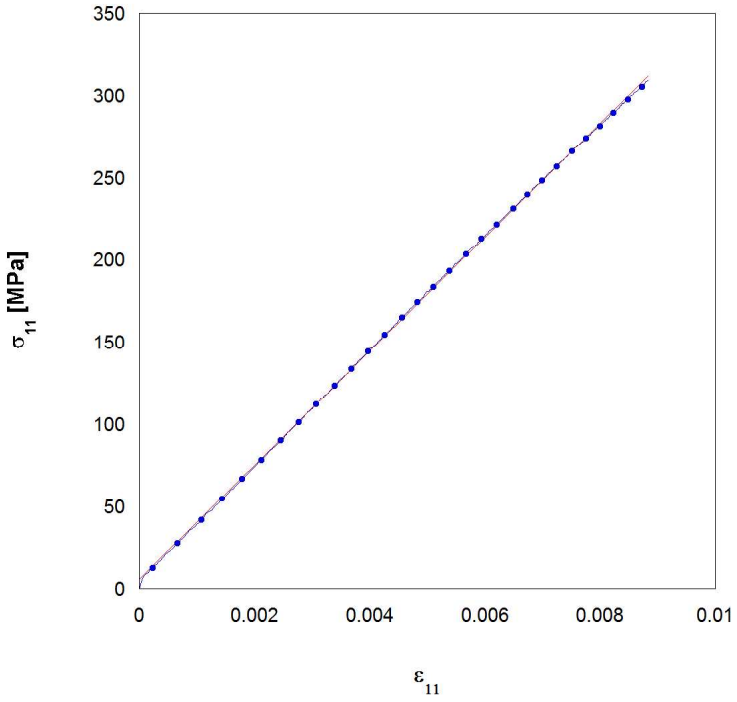

Figure 3: Representative in-plane stress-strain curve along directions 11.

The direction of fibre failure in Fig. 4 is identified at 0° aligned with direction 3 since buckling was not observed. That explains that the strains recorded in both faces were identical. Assuming the cross section of the specimens remained constant during testing and using the force data recorded, the failure compressive stress can be calculated as the ratio between the maximum force and the area of the cross section. The new properties determined in this work are listed in Table 2.

Figure 4: Failure direction of the tested specimen.

Table 2: Properties determined from the original characterisation tests performed in this work.

Property	**Nomenclature**	**Quasi-static Value**	**Dynamic Value**
Shear modulus in directions 23 and 13 [GPa]	$G_{23} = G_{13}$	0.48	0.72
Compressive failure strength in directions 11 and 22 [MPa]	$X_{11_c} = X_{22_c}$	309	928
Shear failure matrix strength in directions 12, 23 and 13 [MPa]	$S_{12_s} = S_{23_s} = S_{13_s}$	120	180

3. Numerical modelling

To characterise the ballistic response of thin GFRP laminates, a fully three-dimensional numerical model was developed. The constitutive response of the glass-fibre composite is defined by means of a continuum damage model that takes into account the different failure mechanisms described by Alonso et al. (2018a). The model is formulated for dynamic analysis and explicit integration and is coded as an Abaqus/Explicit VUMAT user-subroutine. In order to capture the interply damage, a cohesive damage model is also implemented to account for delamination.

3.1. Intralaminar damage model

A continuum damage mechanics approach using different criteria for the onset of damage based on previous failure criteria is implemented. The model defines the failure for the different energy absorption mechanisms separately. Evolution of damage is implemented by a phenomenological softening function controlled by the fracture toughness of the material along each direction. The mechanical response is assumed to be linear-elastic up to the onset of damage and the compliance matrix is written using Voigt's notation as:

$$\begin{bmatrix} \varepsilon_{11} \\ \varepsilon_{22} \\ \varepsilon_{33} \\ \gamma_{12} \\ \gamma_{23} \\ \gamma_{13} \end{bmatrix} = \begin{bmatrix} \frac{1}{E_{11}(1-d_1)} & -\frac{\nu_{21}}{E_{22}} & -\frac{\nu_{31}}{E_{22}} & 0 & 0 & 0 \\ -\frac{\nu_{12}}{E_{11}} & \frac{1}{E_{22}(1-d_2)} & -\frac{\nu_{32}}{E_{33}} & 0 & 0 & 0 \\ -\frac{\nu_{13}}{E_{11}} & -\frac{\nu_{23}}{E_{22}} & \frac{1}{E_{33}(1-d_3)} & 0 & 0 & 0 \\ 0 & 0 & 0 & \frac{1}{G_{12}(1-d_4)} & 0 & 0 \\ 0 & 0 & 0 & 0 & \frac{1}{G_{23}(1-d_5)} & 0 \\ 0 & 0 & 0 & 0 & 0 & \frac{1}{G_{13}(1-d_6)} \end{bmatrix} \begin{bmatrix} \sigma_{11} \\ \sigma_{22} \\ \sigma_{33} \\ \sigma_{12} \\ \sigma_{23} \\ \sigma_{13} \end{bmatrix} \tag{3}$$

where E_{ij}, ν_{ij} and G_{ij} are the Young's moduli, Poisson's ratios and shear moduli associated to $i = 1, 2, 3$ and $j = 1, 2, 3$ directions. The damage parameters d_i (with $i = 1, 2, 3, 4, 5, 6$) are associated with different failure mechanisms and modify the stiffness matrix inducing a phenomenological softening by decreasing decreasing the stress associated to the corresponding damage variable, for example, growth of d_1 implies a decrease in σ_{11} stress. The stress in direction ii is mainly affected by d_i. The damage parameters are controlled by lamina stresses of each individual ply. At every time step, a trial stress state is computed

considering the elastic definition of the material. Afterwards the trial stress is evaluated against the failure envelope, composed by five failure functions, corresponding to the different damage modes:

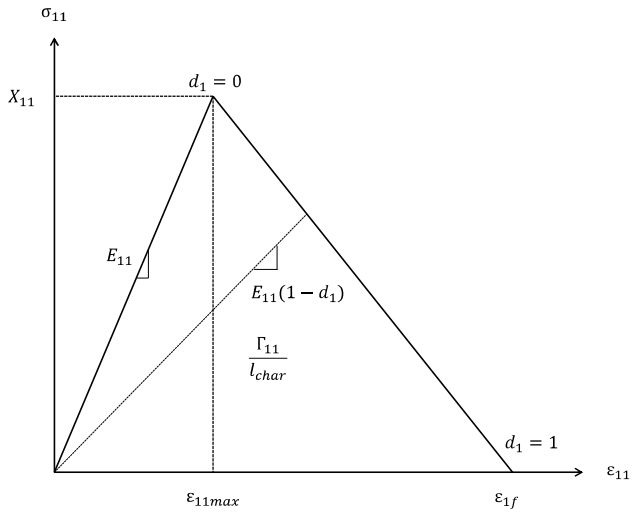

Figure 5: Constitutive description of the implemented softening behaviour.

The fibre failure criterion for woven laminates derives from the model proposed by Chang and Chang (1987) which has been widely used in the literature Iannucci and Willows (2005), López-Puente et al. (2008), Hou et al. (2000). It can be described by

$$\left(\frac{\sigma_{11}}{X_{11i}}\right)^2 + \left(\frac{\sigma_{12}}{S_{12}}\right)^2 + \left(\frac{\sigma_{13}}{S_{13}}\right)^2 = 1 \tag{4}$$

$$\left(\frac{\sigma_{22}}{X_{22i}}\right)^2 + \left(\frac{\sigma_{12}}{S_{12}}\right)^2 + \left(\frac{\sigma_{13}}{S_{13}}\right)^2 = 1 \tag{5}$$

where $i = t, c$ accounts for tension and compression. The functions of evolution of damage for fibre failure are defined in the following equations:

$$d_1 = d_{1+}\frac{\langle\sigma_{11}\rangle}{|\sigma_{11}|} + d_{1-}\frac{\langle-\sigma_{11}\rangle}{|\sigma_{11}|} \tag{6}$$

$$d_2 = d_{2+}\frac{\langle\sigma_{22}\rangle}{|\sigma_{22}|} + d_{2-}\frac{\langle-\sigma_{22}\rangle}{|\sigma_{22}|} \tag{7}$$

where $\langle x\rangle$ is the Macaulay operator defined as $\langle x\rangle = (x + |x|)/2$, d_{1+} and d_{2+} are the damage variables associated with longitudinal fibre failure in tension and d_{1-} and d_{2-} in compression. The Macaulay operator allows the damage caused by tension to be treated separately from the damaged caused by compression, as proposed by Lopes et al. (2009). By formulating the damage variables in this way, the effect of crack closure, which may take place during compression, is contemplated. Furthermore, monotonic damage was implemented in the computational model by comparing the current damage value with the previous time-step one and selecting the maximum. The damage variables that account for tension and compression in equations (6) and (7) are defined as:

$$d_{i+} = \begin{cases} \frac{\varepsilon_{if}(\varepsilon_{ii}-\varepsilon_{iimax})}{\varepsilon_{ii}(\varepsilon_{if}-\varepsilon_{iimax})}, & \text{if eq. (4) is met for i=t ,} \\ 0, & \text{otherwise.} \end{cases} \tag{8}$$

$$d_{i-} = \begin{cases} \frac{\varepsilon_{ifc}(\varepsilon_{ii}-\varepsilon_{iimaxc})}{\varepsilon_{ii}(\varepsilon_{if}-\varepsilon_{iimaxc})}, & \text{if eq. (4) is met for i=c ,} \\ 0, & \text{otherwise.} \end{cases} \tag{9}$$

where $i = 1, 2$ accounts for directions 11 and 22, the subindex c accounts for compression and ε_{if}, ε_{iimax} are defined in Fig. 5 and ε_{ii} is the current applied strain. Although the method is the same, all damage evolution functions are defined as in equation (8) with their respective strains. Note that the behaviour is not as simple as in Fig. 5 because in equation (4) three different stresses are contributing. Eqs. (10) and (11) describes the remaining damage variables:

$$d_3 = \begin{cases} \frac{\varepsilon_{3f}(\varepsilon_{33}-\varepsilon_{33max})}{\varepsilon_{33}(\varepsilon_{3f}-\varepsilon_{33max})}, & \text{if eq. (14) is met,} \\ 0, & \text{otherwise.} \end{cases} \tag{10}$$

$$d_k = \begin{cases} \frac{\varepsilon_{ijf}(\varepsilon_{ij}-\varepsilon_{ijmax})}{\varepsilon_{ij}(\varepsilon_{ijf}-\varepsilon_{ijmax})}, & \text{if eq. (13) is met for k=4 and (15) is met for k=5,6,} \\ 0, & \text{otherwise.} \end{cases} \tag{11}$$

where k, i, j can adopt the following values: $(k = 4, i = 1, j = 2)$, $(k = 5, i = 2, j = 3)$ and $(k = 6, i = 1, j = 3)$. The stress update procedure is the following: for the case of fibre failure in tension along direction 11, the affected stiffness would be E_{11}; once the failure criterion is met, ε_{11max} and σ_{11max} are obtained. ε_{1f} is the maximum strain, which is controlled by the fracture toughness and the characteristic length of the finite element to ensure the energy dissipated is independent of the discretisation. ε_{1f} is defined by the following equation:

$$\varepsilon_{1f} = \frac{2\mathit{\Gamma}_{11}}{X_{11} l_{char}} \tag{12}$$

The onset of matrix cracking failure criterion or in-plane shear failure mode derives from the principle of progressive failure and damage mechanics proposed by Hashin (1980) and Matzenmiller et al. (1995), respectively, and used by Xiao et al. (2007). However, it is slightly different because the current one is not formulated in strains but in stresses, as described by the relation

$$\left(\frac{\sigma_{12}}{S_{12s}}\right)^2 = 1 \tag{13}$$

This approach, also used by Xiao et al. (2007), considers the shear fibre failure strengths S_{12} to be different from the shear failure matrix strengths S_{12s}, (see Section 2.3). Note that shear is a symmetric failure mode and, therefore, no discussion is presented by means of tension and compression load states. Therefore, this model assumes that the shear damage variables are not influenced by crack closure as in the model proposed by Lopes et al. (2009).

3.1.1. Out-of-plane damage model

The out-of-plane damage model considers two different failure mechanisms described by three damage variables: the through-thickness matrix and fibre failure and the crush failure mode that is associated with shear plugging and through-thickness compression Alonso et al. (2018a). Since this continuum damage model is intended to be used for a wide range of thicknesses, these failure mechanisms are considered from the beginning, taking more importance as long as the ratio laminate thickness/ projectile diameter ($\Pi_e = e/\phi_p$) increases as was demonstrated by Alonso et al. (2018a). As the thickness of the laminate increases, the out-of-plane failure mechanisms increase their importance. The maximum thickness tested in this paper is 6 mm, which corresponds with a ratio $\Pi_e = 0.8$, close to 1 where the out-of-plane failure mechanisms become more relevant Alonso et al. (2018a).

The crush failure criterion due to high through-thickness compressive pressure can be described by the relation

$$\left(\frac{\sigma_{33}}{X_{33}}\right)^2 = 1 \tag{14}$$

A single criterion that activates two damage variables (d_5 and d_6) at the same time is defined to define through-thickness matrix and fibre failure,

$$\left(\frac{\sigma_{13}}{S_{13s}}\right)^2 + \left(\frac{\sigma_{23}}{S_{23s}}\right)^2 = 1 \tag{15}$$

Equations (14) and (15) are often combined in one failure criterion, as in the model proposed by Chang and Chang (1987). In this case, however, they are separated to be able to differentiate between the failure caused by compression and the one caused by through-thickness shear stresses. Furthermore, due to the symmetry of the problem, the onset of damage is the same for the activation of parameters d_5 and d_6, although the evolution of damage can be different in later loading stages.

The fracture toughnesses Γ_{ij} (with $i, j = 1, 2, 3$) were estimated from a woven E-glass/epoxy composite by Martínez-Hergueta et al. (2019) and are listed in Table 3.

Table 3: Fracture toughnesses in all directions for the finite element simulations.

Units	Γ_{11}	Γ_{22}	Γ_{33}	Γ_{12}	Γ_{23}	Γ_{13}
N/mm	30	30	100	5	30	30

3.1.2. Interlaminar damage model

The interlaminar damage model implemented has been already used for similar woven laminates by Martínez-Hergueta et al. (2019). Delamination between layers is simulated using a classical cohesive zone method. The behaviour of the cohesive element used is controlled by a traction-separation law as described by Turon et al. (2007). Damage is assumed to initiate when a quadratic interaction function involving the nominal stress ratios reaches a value of one (Abaqus6.14 (2014)),

$$\left(\frac{\langle t_n \rangle}{N}\right)^2 + \left(\frac{t_s}{S}\right)^2 + \left(\frac{t_t}{S}\right)^2 = 1 \tag{16}$$

where t_n, t_s and t_t are the normal and shear stresses, respectively, and N, S are the damage threshold normal and shear strengths of the cohesive elements. As only tensile stresses can lead to delamination, damage cannot be initiated under a pure compressive load. For this reason the Macaulay operator is included in equation (16).

Once the damage criterion is met, the evolution of damage is ruled by the interply fracture toughness Γ^C through the Benzeggagh-Kenane (BK) fracture criterion (Kenane and Benzeggagh (1997)), which takes into account the fracture energy dissipation on the mode mixity,

$$\Gamma^C = \Gamma_n{}^C + (\Gamma_s{}^C - \Gamma_n{}^C)\left(\frac{\Gamma_s + \Gamma_t}{\Gamma_n + \Gamma_s + \Gamma_t}\right)^\eta \tag{17}$$

where $\Gamma_n{}^C$ and $\Gamma_s{}^C$ are the critical energy release rates for delamination in modes I and II, which correspond to pure tension and shear mode, respectively. Γ_n, Γ_s and Γ_t account for the work dissipated due to the displacements along the normal and shear directions, caused by normal and shear stresses, respectively. η is a characteristic parameter of the BK law that accounts for the increase in toughness with the mode mixity (Abaqus6.14 (2014)).

The strength related properties used in the cohesive elements have been estimated from the properties of the resin that serves as adhesive between plies and they are published in García-Castillo (2007). Regarding the fracture toughnesses, the values given by Muñoz et al. (2015) and Martínez-Hergueta et al. (2019) have been taken as reference to avoid numerical problems since the energy absorption by delamination is negligible compared to the energy dissipated by interlaminar failure modes (Muñoz et al. (2015)). Interply properties are collected in Table 4.

Property	Nomenclature	Value
Normal Interface Strength [MPa]	N	55
Shear Interface Strength [MPa]	S	55
Mode I fracture toughness [N/mm]	${\Gamma_n}^C$	0.01
Mode II fracture toughness [N/mm]	${\Gamma_s}^C$	0.01
Benzeggagh-Kenane parameter	η	1.75

Table 4: Mechanical properties of the cohesive elements.

3.2. Definition of the numerical model

The finite element simulations were carried out with four models using Lagrangian 3D elements. The dimensions of the simulated plates are the same as in the experimental tests (150×150 [mm^2]) with thicknesses of 3 and 6 mm. Additionally, two more models were developed, corresponding to thicknesses of 1.8 and 4.2 mm in order to test the evolution of the energy absorption mechanisms with the increase in thickness. The tests with experimental correspondence (3 and 6 mm) were carried out by Buitrago-Pérez et al. (2010). Reduced integration solid elements were used (Abaqus C3D8R) to simulate the plies. Cohesive elements were also used between plies, one element along the thickness direction for each pair, with a thickness of 0.001 mm (Abaqus COH3D8). The target sweep mesh developed is shown in Fig. 6, where 6, 10, 14 and 20 elements were used along the thickness for plates of 1.8, 3, 4.2 and 6 mm thick, respectively. The longitudinal element density meets the criterion established by Abaqus6.14 (2014) when modelling structures under bending loads. The mesh is divided in two regions, a finer mesh where elements of $0.5 \times 0.5 \times 0.3$ [mm^3] are spread out in a 40×40 [mm^2] square, where the projectile impacts. To computational efficiency, a size gradient can be observed in Fig. 6, increasing the size of elements outwards from the impact location. The mesh characteristics are listed in Table 5.

Table 5: Type and number of elements used in the definition of the numerical models for the four thicknesses.

Thickness [mm]	**Refined region**		**Total**
	C3D8R	COH3DR	
1.8	38400	12800	89640
3	64000	25600	167790
4.2	89600	38400	224940
6	128000	57600	344984

A convergence study varying the areal mesh density was carried out, obtaining an optimum that can be seen in Fig. 6.

The spherical projectile, with density 7800 kg/m^3 and diameter 7.5 mm, was simulated with an analytical surface since no permanent deformations were observed on the projectiles after any of the experimental tests. The frictional behaviour between bodies was simulated through the implementation of an exponential decay friction model instead of the classic Coulomb model. In this model the static friction coefficient corresponds to zero slip rate, and the kinetic friction coefficient corresponds to the highest slip rate (Abaqus6.14 (2014)). This model assumes and exponential decay between these two values and is indicated for a wide range of impact velocities. The friction coefficient at any slip rate is given by

$$\mu = \mu_k + (\mu_s - \mu_k)e^{-d_c \dot{\gamma}_{eq}} \tag{18}$$

where μ_k is the kinetic friction coefficient, μ_s is the static friction coefficient, d_c is a user-defined decay coefficient, and $\dot{\gamma}_{eq}$ is the slip rate. Given a static value and two points of the curve, the model can be defined. This ensures that the horizontal asymptote for the highest slip rate gives a low friction coefficient ($\mu_k \simeq 0.01$) and the friction coefficient for the lowest impact velocity of the experiments is $\mu = 0.3$. This

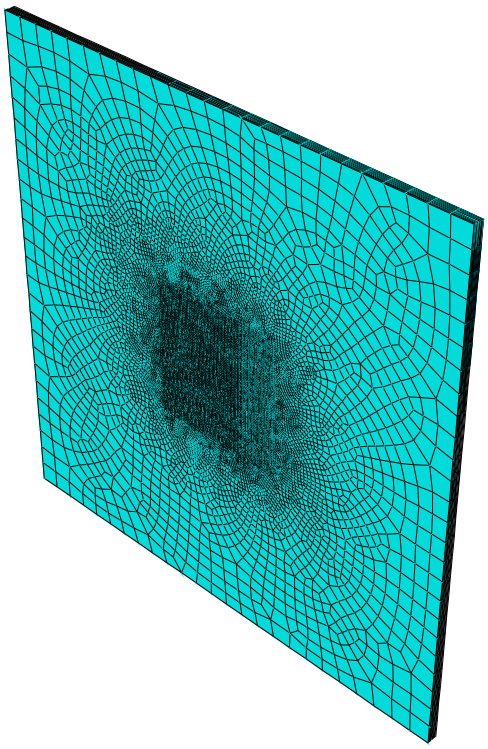

Figure 6: Example of finite element discretisation used in the numerical models.

exponential decay friction model has been used by other authors in plain-woven composites Briesciani et al. (2016). The boundary conditions applied to the model are: (i) the laminate edges nodes fixed and (ii) an initial velocity given to the projectile. The elements are removed when any of the damage variables reaches the threshold value of 1.

4. Validation

This section presents and discusses the results obtained with the proposed numerical model in terms of the ballistic performance. To this end, the numerical model is validated with experimental residual velocities. In the impact tests carried out by Buitrago-Pérez et al. (2010) for 3 and 6 mm thick specimens, laminates of 150×150 [mm^2] were clamped in a testing frame. The 7.5 mm diameter steel spherical projectile was propelled by a pressurised helium chamber against the laminate. The ballistic response predicted by the finite element model and the experimental results from the literature (Buitrago-Pérez et al. (2010)) are shown in Fig. 7.

Good agreement is observed between the experimental data and the finite element results for both the ballistic limit and the residual velocities, as shown in Fig. 7. In order to obtain the experimental ballistic limit, the experimental data curve was adjusted using the Lambert-Jonas equation (Lambert and Jonas (1976)),

$$v_r = A\left(v_i^p - v_{bl}^p\right)^{\frac{1}{p}} \tag{19}$$

where A and p are empirical parameters. The ballistic limits predicted by the numerical model matches the experimental results with a maximum error of 7%. This discrepancy in the ballistic limit could be provoked by possible variations in the fracture thoughnesses since they have been estimated. The highest error is reached at the maximum velocity for a thickness of 6 mm but it is below the 17%. Predictions could be

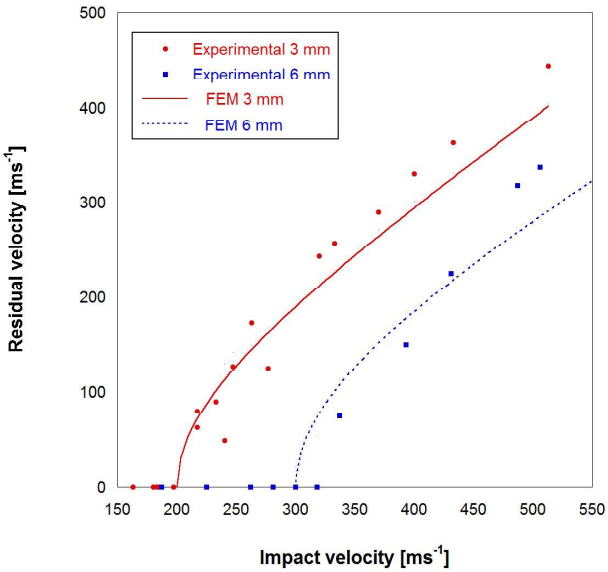

Figure 7: Experimental (Buitrago-Pérez et al. (2010)) and finite element ballistic limit plots.

worse at higher velocities due to the higher temperatures induced at the impact point and the degradation of the glass fibre (Hufenbach et al. (2011), Bai et al. (2008)).

In order to fully validate the model it is also necessary to show that the failure modes in the finite element model are equivalent to the experiments. To do so, different failure modes were identified on the specimens: failure of fibres, delamination, matrix cracking, compression and shear plugging. To show a representative example, front and rear faces of a 3 mm thick specimen impacted at a velocity of 247 m/s are shown in Fig. 8.

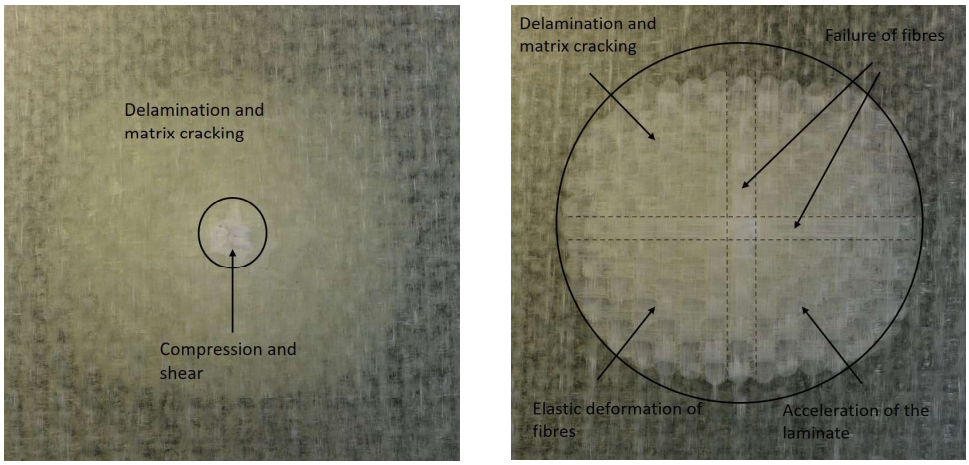

(a) *(b)*

Figure 8: Front (a) and rear (b) faces of the 3 mm thick specimen impacted at 247 m/s with the failure mechanisms highlighted.

Compression is more evident in a small area on the front face around the impact location, as can be seen in Fig. 8, as compression is a localised failure mode that takes place just below the projectile. The fibres marked in Figure 8a fail by compression and shear plugging mechanisms. This failure modes are activated

by the normal stresses arising along the thickness direction and the shear stresses generated in the periphery of the projectile, respectively. Delamination and matrix cracking can also be observed in both the front and the rear faces. The damaged area is wider in the rear face, which can be explained because it is the zone withstanding more bending when the laminate accelerates, contributing to further detachment of the plies. The zone affected by the acceleration of the laminate also absorbs energy (recoverable) by elastic deformation of fibres and tensile failure of fibres. The fibres that fail under direct tension are highlighted in black in Fig. 8. These fibres, together with the others inside the circle, also absorb elastic (recoverable) energy during impact. After going through the visual inspection of the specimens, it can be concluded that failures modes considered in the finite element model capture the main observed damage mechanisms. Depending on the specimen and the impact velocity, some of the failure mechanisms are more or less evident when the specimens are visually inspected.

5. Results

5.1. Ballistic response

In addition, simulations of two more thicknesses were carried out in order to determine the ballistic response of laminates for a wider range of thicknesses. Figure 9 shows the ballistic limit plots for all numerical models.

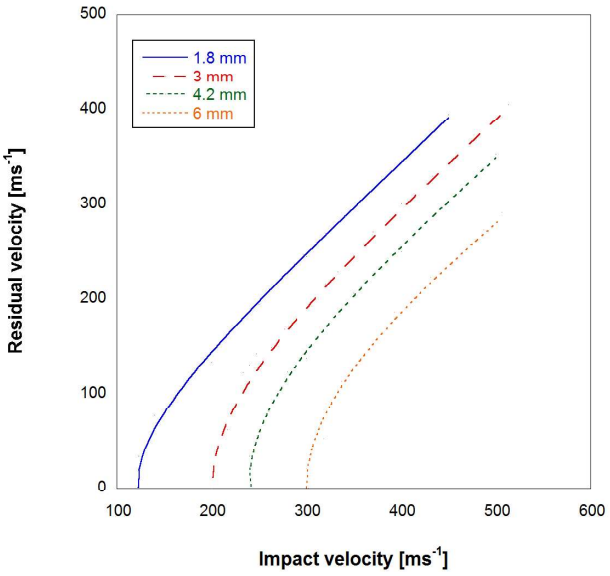

Figure 9: Ballistic limit plots for all numerical models: 1.8, 3, 4.2 and 6 mm.

A good agreement is observed in the ballistic limit between the experimental results and the predictions made by the finite element model for 3 and 6 mm, with relative differences lower than 7%. Although no experimental results are available for the 1.8 and 4.2 mm specimens, a close to linear relationship is observed between the plate thickness and the ballistic limit for all laminates within a range of 3 to 12 mm, as was demonstrated by Alonso et al. (2018b). Consequently, if the ballistic limit for these thicknesses is close to linear, a good agreement with hypothetical experiments can be assumed. For the 4.2 mm thick specimen the ballistic limit is close to the experimental (7.1% relative difference), and therefore a good agreement with the experiments can be assumed. No experimental results are available for thicknesses under 3 mm, so no conclusions can be drawn for the ballistic limit for 1.8 mm specimens.

5.2. Failure mechanisms, energy absorption and damaged surface

The different failure mechanisms captured by the finite element model were discussed in the previous paragraphs. As the FE model accounts for all failure mechanisms in theory, it is interesting to see if it can predict the morphology of the damaged surface of the laminates. To this end, three different cases around the ballistic limit for 3 and 6 mm are presented and discussed in this section.

Fig. 10 shows the front damaged surface of a real specimen (10a) and the mid-plane cut predicted by the finite element model (10b). The front of the damaged surface in all specimens is similar to the examples in Fig. 10. The finite element model accurately predicts this fracture mode, both morphologically and quantitatively. This surface is of comparable size in the specimens and in the finite element model, and its dimension is similar to the projectile. It is logical since the local phenomenon of compression takes place just underneath the projectile.

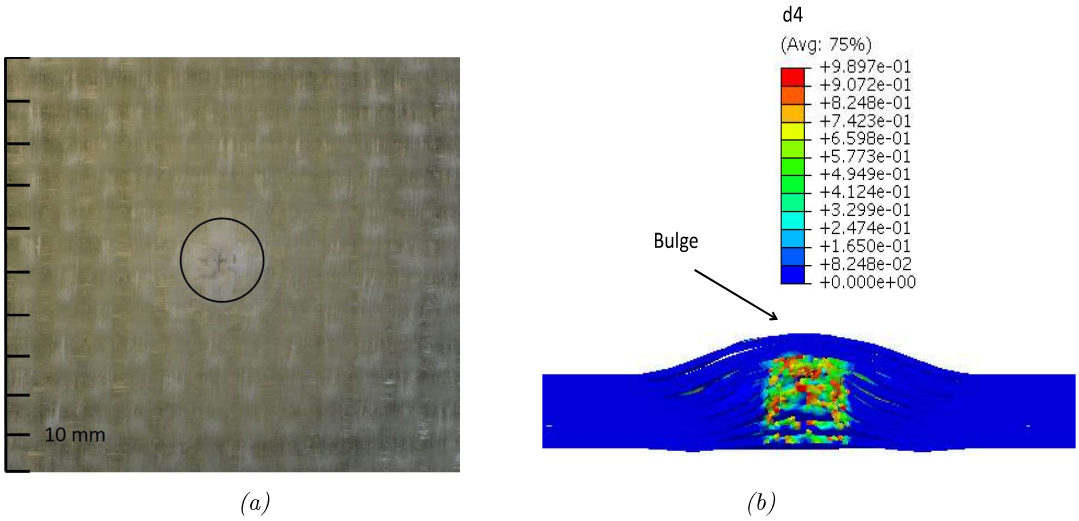

(a) *(b)*

Figure 10: (a) Experimental damaged front surface and (b) numerical mid-plane cut representing the damage variable d_4, for a 6 mm thick specimen impacted at 300 m/s at 0.05 ms.

The general pattern of the damage on the back face is shown in Fig. 8. Figures 11a and 11b show the front and back face damaged surface for the 3 mm thick specimen impacted at a velocity near the ballistic limit. The shape of the rear damaged surface is similar experimentally and numerically for 6 mm thick specimens as shown in Figs. 8 and 11. The langrangian strain LE11 and LE22 are represented in Fig. 11 since they are the most energetic. All specimens follow a similar trend, showing the breakage of the main four fibres (within the contact region with the projectile) as is usual in this woven laminates. The damaged surface presents this shape because these fibres on the back face withstand larger deformations as the representation of LE11 and LE22 shows before failing in tension. The finite element model simulations reproduce well this behaviour, as can be seen in Figures 11b and 11d. Apart from the failure of fibres on the back face (see Fig. 11), it is observed that an acceleration of the laminate has taken place. The formation of the bulge is a consequence of the membrane like behaviour of thin laminates. Experimentally, it can be inferred from the delaminated area on the back face of the laminate. In Fig. 10b a numerical image with a mid-plane cut shows the damage variable d_4 related to matrix cracking, which is a consequence of the bulge formation during the impact.

The damaged areas on the back faces as predicted by the finite element model are compared to the experimental damaged areas in Fig. 12 for the 3 mm thick specimens at different impact velocities. Fig. 12 shows the general trend of the finite element simulations in concordance with experimental results regarding the extension of the damaged (delaminated) area. The same trend can be experimentally appreciated in

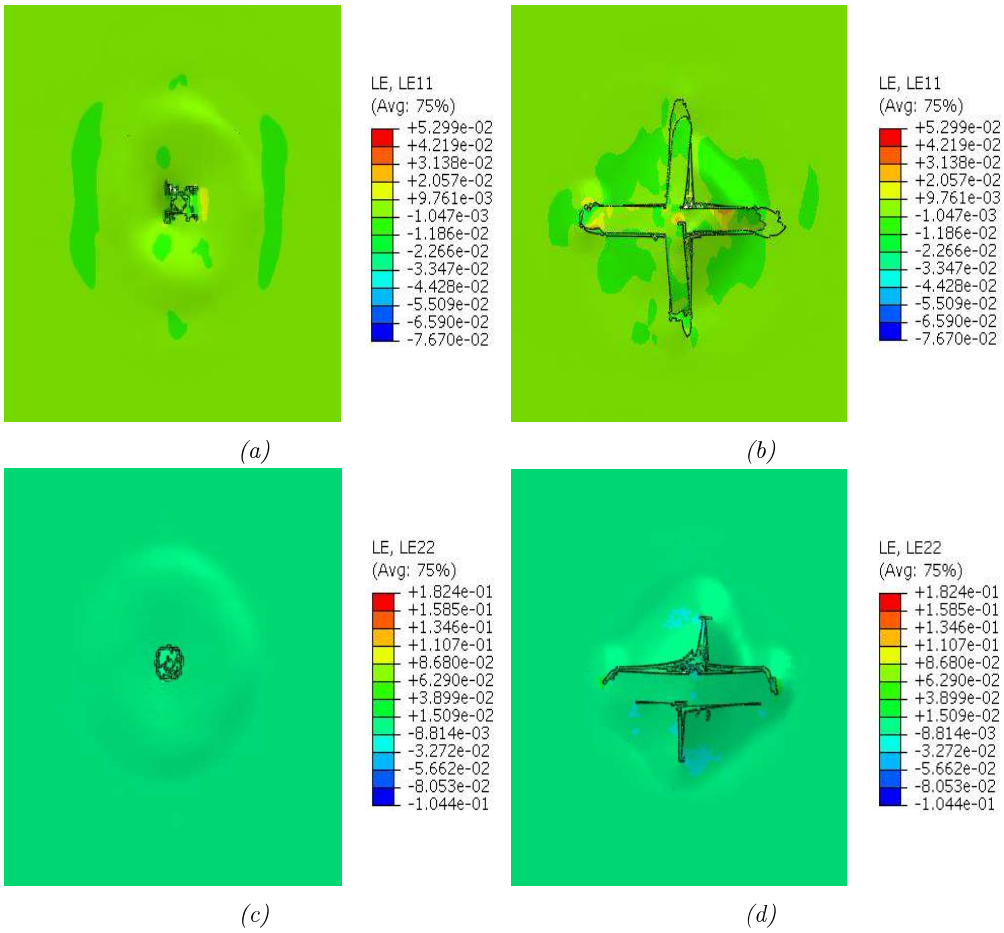

Figure 11: Representation of the langrangian strain (LE11 for a), b) and LE22 for c), d)) on the front and back faces, for (a, b) 3 mm and (c, d) 6 mm thick specimens impacted at (a, b) 217 m/s and (c, d) 300 m/s at 0.11 ms.

the study carried out by Alonso et al. (2018b). This extension grows as impact velocities get closer to the ballistic limit and are smaller for other impact velocities. This happens because one of the main causes that provokes delamination is the transverse wave causing the bending of the laminate. Since the contact time is maximum at the ballistic limit, the distance travelled by the transverse wave is also maximum and thus the delaminated area.

The damaged surface of the tested laminates should be quantitatively related to the qualitative observations from the finite element model (e.g. failure mechanisms and energy absorption mechanisms). To capture the contributions of the different energy absorption mechanisms, eight cases were analysed: two for each thickness at impact velocities close to the ballistic limit and slightly above. This allowed for the evolution and relevance of the different energy absorption mechanisms to be observed.

One important assumption in the finite element models was to associate the failure criteria to the energy-absorption mechanisms defined in the theoretical model of Alonso et al. (2018a). This ensures the failure criteria in the numerical model are associated to failure modes or energy absorption mechanisms in the theoretical model. In this section the amount of energy absorbed for each mechanism is analysed. Fibre failure (see equations (4) and (5)) is associated to elastic deformation and tensile failure of fibres in the theoretical model. Matrix failure (see equation (14)) is associated with matrix cracking and crush failure and failure caused by shear stresses (see equations (13) and (15)) are associated to compression and shear

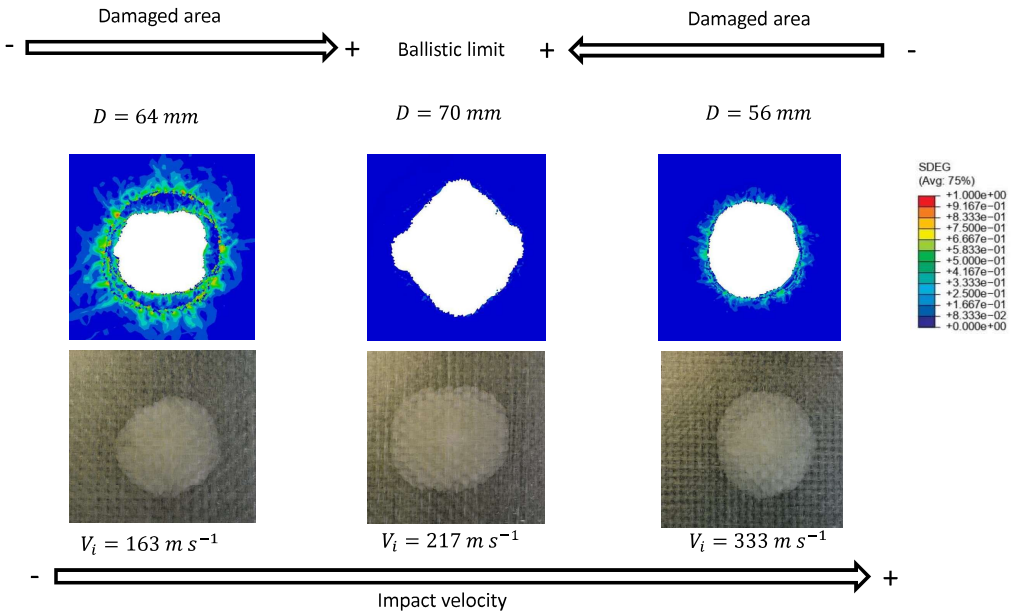

Figure 12: Numerically predicted damaged for increasing impact velocities for the 3 mm thick specimens.

plugging, respectively. This numerical study is carried out to analyse the general trends of the energies absorbed in the numerical model. The energy of each element is calculated with the following procedure: when the element is removed due to a damage variable having reached the threshold value of 1, the energy related to this failure criterion is the energy below the stress-strain curve and is dissipated. At that point, however, the stress-strain curve in the other directions may not be zero, so the elastic and dissipated energies in those directions have to be taken into account at the moment of deletion. For example, if $d_1 = 1$ in one element and at that point in direction 33 we are in the black point (the end of $\vec{b}$) which Fig. 13 shows, the energy in direction 33 is calculated as the sum of the elastic energy plus the dissipated energy. It should be noted that these are specific energy components that have to be multiplied by the volume of the element. Once all the energies of all the elements are calculated, they can be normalised with the initial kinetic energy of the projectile. Since all the points in the constitutive relation are defined, the generic expressions to calculate the plastic and the elastic energies at any moment are the following:

$$E_e = \frac{1}{2} \mid \vec{a} \times \vec{b} \mid \tag{20}$$

$$E_d = \frac{1}{2} \mid \vec{b} \times \vec{c} \mid \tag{21}$$

where E_e is the elastic energy, E_d is the dissipated energy, $\vec{a}$, $\vec{b}$ and $\vec{c}$ are the vectors shown in Fig. 13, and $\times$ is the vector product.

The study of the energies has been carried out at velocities around the ballistic limit for the four thicknesses. The energy contributions considered are coupled with the failure criteria as explained in the finite element model. These energy-absorption mechanisms are: in-plane fibre failure of fibres, compression along the thickness direction, matrix cracking and delamination, shear plugging, which includes the out-of-plane shear failure, kinetic energy provoked by the acceleration of the laminate and friction between the impactor and the plate. The energy provoked by the acceleration of the laminate cannot be understood as dissipative but as an energy transferred from the projectile. In this regard, we have not taken this energy into account in Figs. 14 and 15. The velocity which determines if the perforation takes place or not is the most important to ensure safety and structural integrity in any application. That is why the cases shown in Table 6 are analysed.

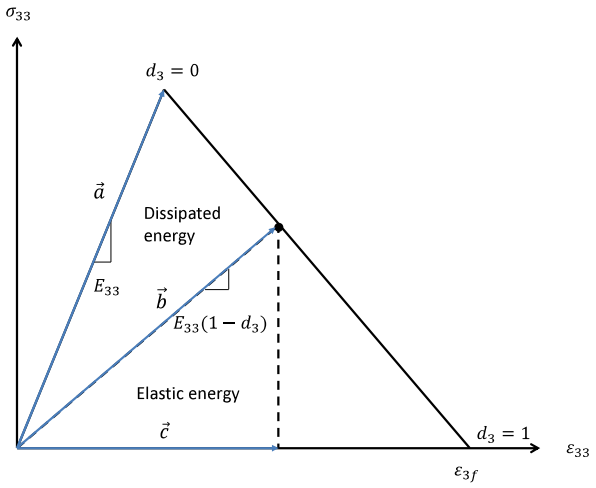

Figure 13: Element deletion scheme and relation to how the energy terms are computed in the numerical model.

Table 6: Impact velocities used to analyse the energy absorption mechanisms in the finite element model.

Thickness [mm]	**Impact velocity 1** [m/s]	**Impact velocity 2** [m/s]
1.8	140	180
3.0	197	240
4.2	240	280
6.0	318	337

The absorbed energy predicted by the numerical model for 1.8 and 3 mm thick specimens is shown in Figs. 14a and 14b.

Figs. 14a and 14b show that for thin laminates the dominant energy absorption mechanism is the breakage and deformation (recoverable) of fibres, as the damaged surfaces confirm (Figs. 11). Considering that these are thin laminates, it is logical that significant energy is absorbed by this mechanism since it has been observed experimentally that the behaviour is similar to a membrane (Moyre et al. (2000), Naik and Shrirao (2004)). Therefore, the deformation of fibres is high before the failure. For an impact velocity of 140 m/s the contribution of breakage and deformation of fibres is more than twice the following energy-absorption mechanism, as shown in Fig. 14a. Additionally, compression is low because at the ballistic limit the contact time, and thus the deformation of the laminate before failure, is maximum, resulting in fibre breakage. Figures 14a and 14b also show that matrix cracking and shear plugging are minor energy absorption mechanisms. Furthermore, the energy absorbed by friction is low due to the thickness of the laminates. For an impact velocity of 240 m/s it can be seen that compression starts to compete with fibre failure (see Fig. 14b).

The absorbed energies predicted by the finite element model for 4.2 and 6 mm thick specimens is shown in Figs. 15a and 15b. Fig. 15a shows that the most relevant mechanism in this case is still fibre failure. However, a tendency to increase the importance of out-of-plane mechanisms can be observed since compression becomes more relevant with the increase of the thickness. Also, shear plugging becomes more important (see Figure 15a) than for thinner specimens, as can be observed in Figs. 14a and 14b. This tendency can be confirmed from the results in Fig. 15b. Compression is the most important energy absorption mechanism followed by fibre failure for the 6 mm thick specimens. Experimentally, compression can be clearly seen in the first layers in these specimens, as shown in Figs. 10a and 10b. For the 4.2 and 6 mm thick specimens,

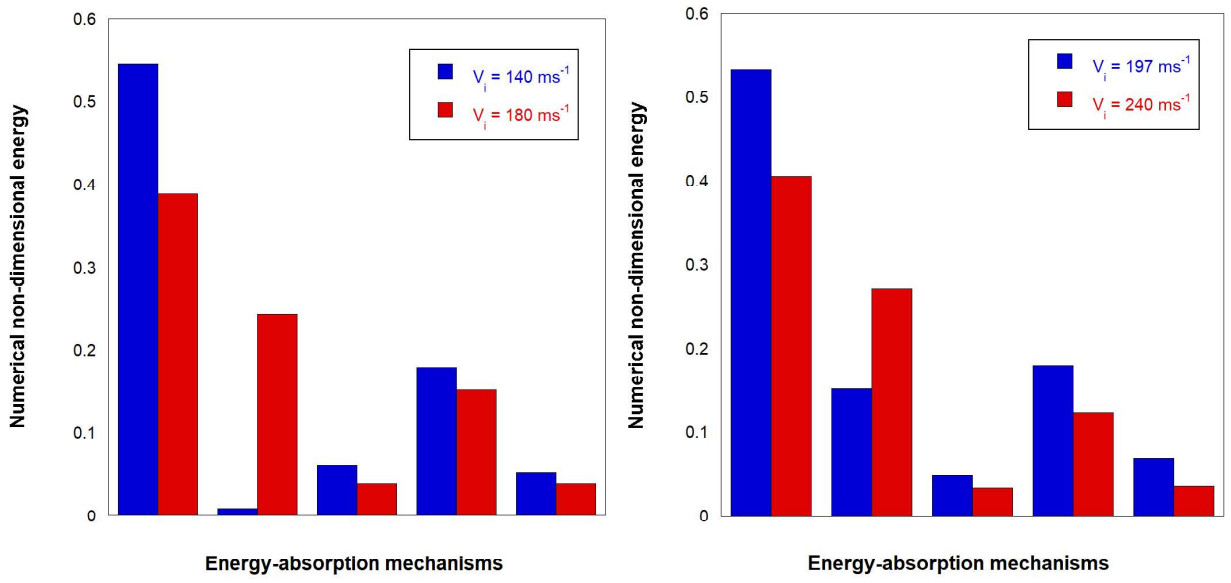

(a) *(b)*

Figure 14: Numerical non-dimensional energy fractions from left to right: Failure of fibres, compression, matrix cracking, shear plugging and friction for: (a) 1.8 mm thick specimen at impact velocities of 140 m/s (blue) and 180 m/s (red); (b) 3 mm thick specimen at impact velocities of 197 m/s (blue) and 240 m/s (red).

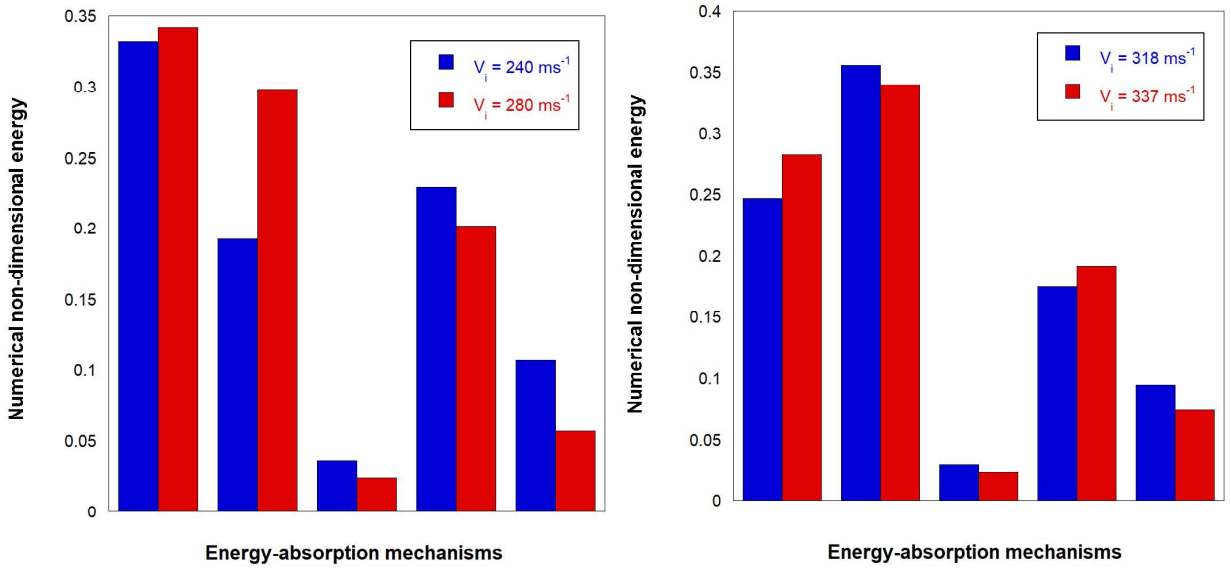

(a) *(b)*

Figure 15: Numerical non-dimensional energy fractions from left to right: Failure of fibres, compression, matrix cracking, shear plugging and friction for: (a) 4.2 mm thick specimen at impact velocities of 240 m/s (blue) and 280 m/s (red); (b) 6 mm thick specimen at impact velocities of 318 m/s (blue) and 337 m/s (red).

the out-of-plane mechanisms (compression and shear plugging) acquire an important role, being dominant for the case of 6 mm. For thicker laminates, bending effects become less evident and diminish the movement

of the laminate. In this situation, the impact face layers absorb more energy by compression whilst fibre failure dominates on the back face. It should be noted that friction increases its importance with thickness, albeit always being a small contribution (below 10%). The artificial energy is lower than 5% in all cases.

The 6 mm thick specimen seems to be at the transition point regarding the energy absorption mechanisms. Fibre failure is still one of the most relevant energy absorption mechanisms but shared with compression failure. These observations are consistent with the hypotheses assumed in the theoretical model and the results presented by Alonso et al. (2018a). As long as the thickness increases, the phenomena of compression and shear stresses become more relevant. For the laminates tested in this work, the thin-thick laminate threshold is approximately 7 mm (for the used projectile), as demonstrated by Alonso et al. (2018a). Therefore, it should be expected that these out-of-plane mechanisms become more important in the 6 mm plates, as the assumption of thin laminates becomes less valid.

6. Conclusions

In this work, the high-velocity impact phenomenon on thin woven E-glass fibre/polyester composites was studied by means of a finite element model. Original shear and in-plane compression tests were carried out in order to obtain the properties needed for the numerical modelling. All the material properties used and obtained in this work have a clear physical meaning and can be obtained from specific experimental tests. A finite element model was implemented in a VUMAT user sub-routine in Abaqus/Explicit. The model was implemented using Langrangian 3D elements, trilinear elements with reduced integration and cohesive elements to account for delamination. A continuum damage model was defined to separate the in-plane damage from the out-of-plane damage to take into account effects when the thickness increases. The failure criteria of the finite element model are a mixture of different criteria previously used. The failure mechanisms in the finite model are associated to different energy absorption mechanisms, as defined in the classic analytical models. In this way, a clear relation between stresses and the corresponding failure mechanism is defined. The damage evolution variables are defined as a function of fracture toughnesses.

Experimental and numerical ballistic limits and residual velocities were compared for 3 and 6 mm thick specimens. Good agreement was observed with maximum differences lower than 15%. The more significant differences in the ballistic behaviour occur at higher impact velocities, where the finite element models tend to underestimate the residual velocities, as they do not take into account the degradation of material properties due to the high temperatures. The damaged surfaces were analysed for 3 and 6 mm thick specimens, comparing the experimental tests with finite element simulations. The front damaged surface is in general limited to a small area where compression takes place and shear stresses arise. The rear damaged surface has the typical four-branched shape due to the failure in tension. Additionally, the damaged area on the back faces was compared for impact velocities close to the ballistic limit, with good results in terms of the morphology and in the most of the cases good qualitative predictions for the extension of damage.

The model has been proved to be successful to reproduce the dominant failure models that can be experimentally observed. The comparison of damaged surfaces confirms the capability of the models to accurately predict the main failure modes such as compression on the front face, fibre failure on the rear face or matrix cracking and delamination. An analysis of the energy absorption mechanisms has also been carried out, where it was observed that the most important energy absorption mechanism in very thin laminates is fibre failure. It is an expected observation since the very thin laminate behave as a membrane and the deformation before failure is high. The relevance of compression is lower but increases with the impact velocity and it mainly occurs on the impact face layers. Shear plugging does not play a major role in thin laminates. Friction and matrix cracking together with delamination are the least relevant mechanisms. Out-of-plane energy absorption mechanisms, however, become highly relevant when the thickness increases, until playing a fundamental role for 6 mm thick specimens. Although fibre failure is still one of the main failure mechanisms, compression plays a fundamental role for increasing thicknesses, becoming the most important one for 6 mm thick specimens. The increase of out-of-plane shear stresses leads to a significant increase in shear plugging when compared to thinner laminates. Friction still plays a minor role, although it is clear that friction increases with thickness. Matrix cracking and delamination are the least important failure mechanisms.

7. Acknowledgements

L. Alonso, S.K.Garcá Castillo and C.Navarro are indebted to the project 'Acción Estratégica en Materiales Compuestos y Análisis Numérico simplificado de Estructuras y protecciones ligeras sometidas a impacto balístico' (2010/00309/002) of the University Carlos III of Madrid for the financial support of this work. F. Martínez-Hergueta acknowledges support from PECRE1819_02 from the Scottish Research Partnership in Engineering. D. Garcia-Gonzalez acknowledges support from the Talent Attraction grant (CM 2018 - 2018-T2/IND-9992) from the Comunidad de Madrid.

References

Abaqus6.14, 2014. Systemes D. Abaqus 6.14 User's manual.

Alonso, L., Navarro, C., García-Castillo, S., jun 2018a. Analytical models for the perforation of thick and thin thicknesses woven-laminates subjected to high-velocity impact. Composites Part B 143 (15), 292–300.

Alonso, L., Navarro, C., García-Castillo, S., sep 2018b. Experimental study of woven-laminates structures subjected to high-velocity impact. Mechanics of Advanced Materials and Structures.

Ansari, M., Chakrabarti, A., Iqbal, M., sep 2017. An experimental and finite element investigation of the ballistic performance of laminated gfrp composite target. Composites Part B: Engineering 125, 211–226.

ASTM-Standard-D3410/D-3410M-95, 2010. Standard test method for compressive properties of polymer matrix composite materials with unsupported gage section by shear loading.

Bai, Y., Post, N., Lesko, J., Keller, T., mar 2008. Experimental investigations on temperature-dependent thermo-physical and mechanical properties of pultruded gfrp composites. Thermochimica Apta 469 (1-2), 28–35.

Briesciani, L., Manes, A., Ruggiero, A., Iannitti, G., Giglio, M., mar 2016. Experimental tests and numerical modelling of ballistic impacts against kevlar 29 plain-woven fabrics with an epoxy matrix: macro-homogeneous and meso-heterogeneous approaches. Composites Part B: Engineering 88, 114–130.

Buitrago-Pérez, B., García-Castillo, S., Barbero, E., may 2010. Experimental analysis of perforation of glass/polyester structures subjected to high-velocity impact. Material Letters 64 (9), 1052–1054.

Chang, F., Chang, K., sep 1987. A progressive damage model for laminated composites containing stress concentrations. Journal of Composite Materials 21, 834–855.

Chu, T., Ha-Minh, C., Imad, A., jun 2016. A numerical investigation of the influence of yarn mechanical and physical properties on the ballistic impact behavior of a kevlar km2 woven fabric. Composites Part B: Engineering 95 (15), 144–154.

Corigliano, A., Rizzi, E., Papa, E., 2000. Experimental characterization and numerical simulations of a syntactic-foam/glass-fibre composite sandwich. Composites Science and Technology 60, 2169–2180.

Davila, C., Camacho, P., Rose, C., feb 2005. Failure criteria for frp laminates. Journal of Composite Materials 39 (4), 323–345.

Dayou, M., Manes, A., Campos-Amico, S.and Giglio, M., 2019. Ballistic strain-rate-dependent material modelling of glass-fibre woven composite based on the prediction of a meso-heterogeneous approach. Composite Structures 210, 840–857.

Fatt, M., Lin, C., jul 2004. Perforation of clamped, woven e-glass/polyester panels. Composites Part B 35 (5), 359–378.

García-Castillo, S., 2007. Análisis de laminados de materiales compuestos con precarga en su plano y sometidos a impacto.

García-Castillo, S., López-Puente, J., Sánchez Sáez, S., Barbero, E., Navarro, C., may 2006. Analytical model for energy absorption capabilities of glass/polyester panels subjected to ballistic impact. Conference in Developments in Theoretical and Applied Mechanics.

García-Castillo, S., Sánchez Sáez, S., Santiuste, C., Barbero, E., Navarro, C., 2013. Perforation of Composite Laminate Subjected to Dynamic Loads. Springer Netherlands, pp. 291–337.

Gower, H., Cronin, D., Plumtree, A., sep 2008. Ballistic impact response of laminated composite panels. International Journal of Impact Engineering 35 (9), 1000–1008.

Harding, J., Ruiz, C., 1998. The mechanical behaviour of composite materials under impact loading. Key Engineering Materials 141-143, 403–426.

Harding, J., Welsh, L., 1983. A tensile testing technique for fiber-reinforced composites at impact rates of strain. Journal of Material Science 18, 1810–1826.

Hashin, Z., jun 1980. Failure criteria for unidirectional fiber composites. Journal of Applied Mechanics 47 (2), 329–334.

Hou, J., Petrinic, N., Ruiz, C., Hallet, S., feb 2000. Prediction of impact damage in composite plates. Composites Science and Technology 60 (2), 273–281.

Hufenbach, W., Gude, M., Böhm, R., Zscheyge, M., sep 2011. The effect of temperature on mechanical properties and failure behaviour of hybrid yarn textile-reinforced thermoplastics. Materials & Design 32 (8-9), 4278–4288.

Iannucci, L., Dechaene, R., Willows, M., Degrick, J., mar 2001. A failure model for the analysis of thin woven glass composite structures under impact loadings. Computers Structures 79 (8), 785–799.

Iannucci, L., Willows, M., dec 2005. An energy based damage mechanics approach to modelling impact onto woven composite materials part i: Numerical models. Composites Part A: Applied science and manufacturing 37 (11), 2041–2056.

Kenane, M., Benzeggagh, M., dec 1997. Mixed-mode delamination fracture thoughness of unidirectional glass/epoxi composites under fatigue loading. Composites Science and Technology 57, 597–605.

Lambert, J., Jonas, G., 1976. Towards standarization of in terminal ballistic testing: velocity representation. Ballistic research laboratories.

Lopes, C., Camanho, P., Gürdal, Z., Miamí, P., González, E., jun 2009. Low-velocity impact damage on dispersed stacking sequence laminates. part ii: Numerical simulations. Composites Science and Technology 69 (7–8), 937–947.

López-Puente, J., Zaera, R., Navarro, C., feb 2008. Experimental and numerical analysis of normal and oblique ballistic impacts on thin carbon/epoxy woven laminates. Composites Part A 39 (2), 374–387.

Martínez-Hergueta, F., Ares, D., Ridruejo, A., Wiegand, J., Petrinic, N., feb 2019. Modelling the in-plane strain rate dependent behaviour of woven composites with special emphasis on the non-linear shear response. Composite Structures 210 (15), 840–857.

Matzenmiller, A., Lublinear, J., Taylor, R., apr 1995. A constitutive model for anisotropic damage in fiber-composites. Mechanics of Materials 20 (2), 125–152.

Miamí, P., Camanho, P., Mayugo, J., Dávila, C., oct 2007a. A continuum damage model for composite laminates: Part i–constitutive model. Mechanics of Materials 39 (10), 897–908.

Miamí, P., Camanho, P., Mayugo, J., Dávila, C., oct 2007b. A continuum damage model for composite laminates: Part ii–computational implementation and validation. Mechanics of Materials 39 (10), 909–919.

Moyre, S., Hine, P., Duckett, R., Carr, D., Ward, I., nov 2000. Modelling of the energy absorption by polymer composites upon ballistic impact. Composites Science and Technology 60 (14), 2631–2642.

Muñoz, F., Martínez-Hergueta, F., Gálvez, F., González, C., Llorca, J., sep 2015. Ballistic performance of hybrid 3d woven composites: Experiments and simulations. Composite Structures 127 (1), 141–151.

Naik, N., Doshi, A., 2005. Ballistic impact behaviour of thick composites: Analytical formulation. AIAA Journal 43 (7), 1525–1536.

Naik, N., Shrirao, P., oct–dec 2004. Composite structures under ballistic impact. Composite Structures 66 (1–4), 579–590.

Silva, M., Cisma, C., Chiorean, C., mar 2005. Numerical simulation of ballistic impact on composite laminates. International Journal of Impact Engineering 31 (3), 289–306.

Turon, A., Dávila, C., Camaho, P., Coste, J., jul 2007. An engineering solution for mesh size effects in the simulation of delamination using cohesive zone models. Engineering Fracture Mechanics 74 (10), 1665–1682.

Walter, T., Subhash, G., Yen, C., apr 2009. Damage models in 3d glass fiber epoxy woven composites under high rate of impact loading. Composites Part B 40 (6), 584–589.

Xiao, J., Gama, B., Gillespie Jr, J., apr 2007. Progressive damage and delamination in plain weave s-2 glass/sc-15 composites under quasi-static punch-shear loading. Composite Structures 78 (2), 182–196.

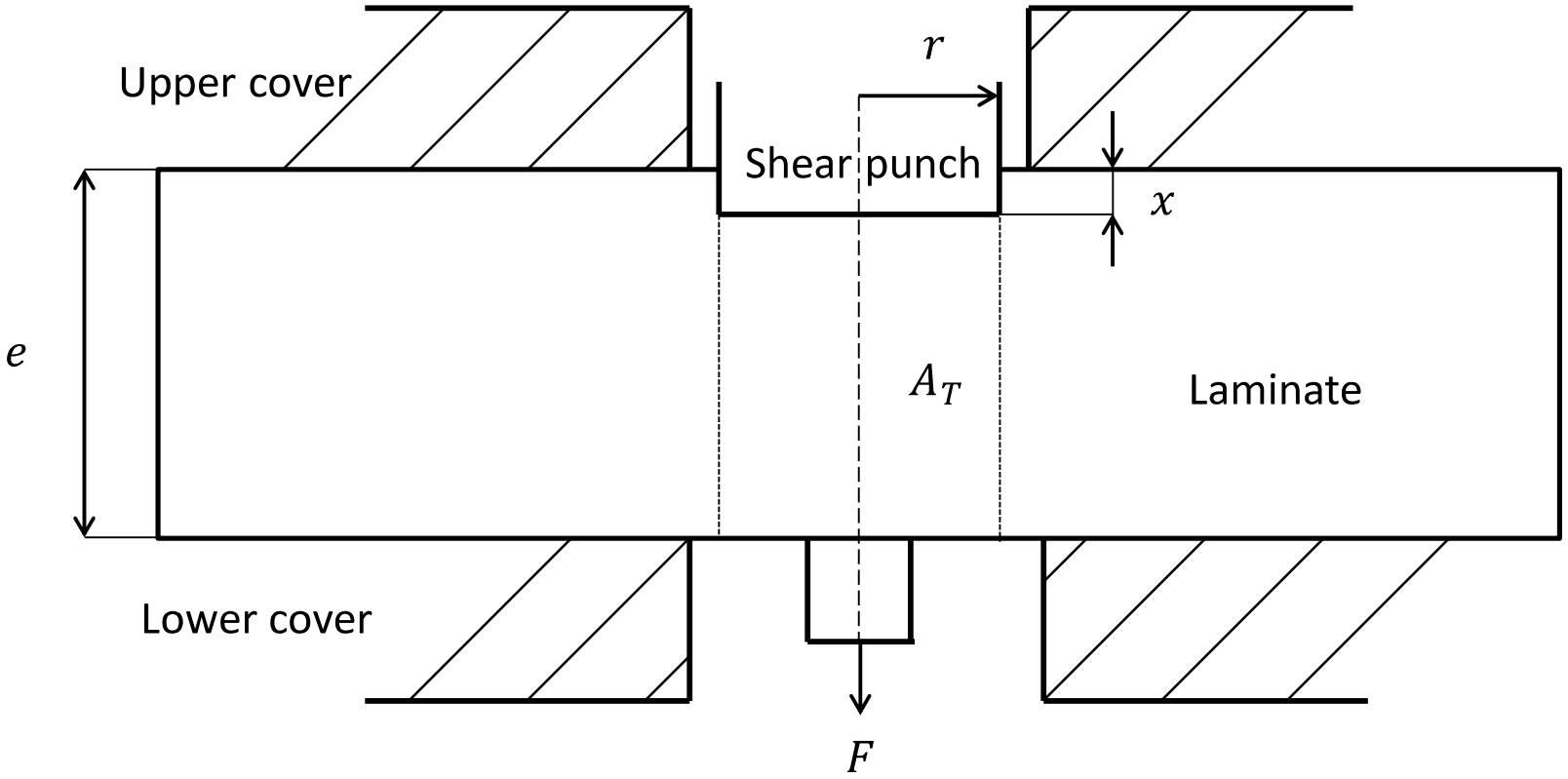
Upper cover
r
Shear punch
x
e
A_T
Laminate
Lower cover
F

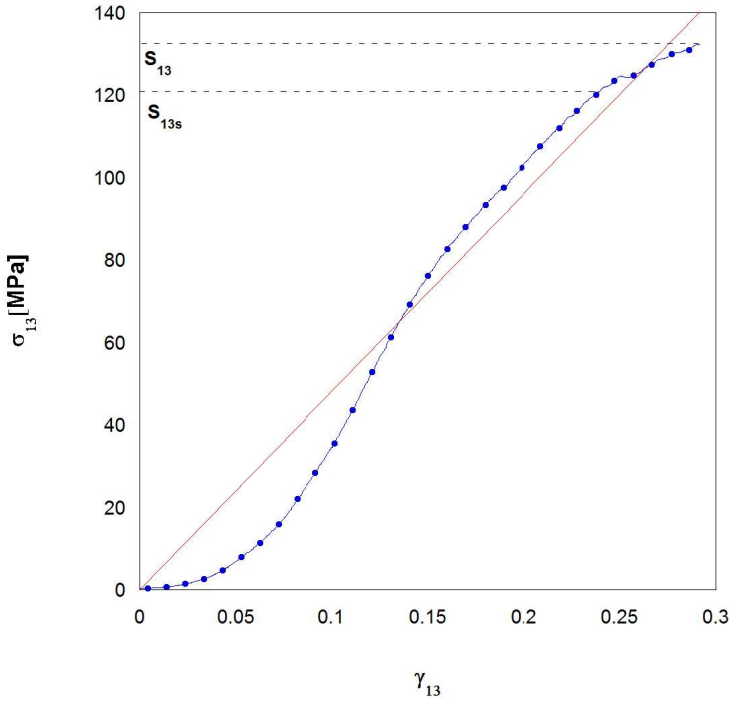
140
120
100
80
60
40
20
0
0
0.05
0.1
0.15
0.2
0.25
0.3
S13
S13s
σ13 [MPa]
γ13

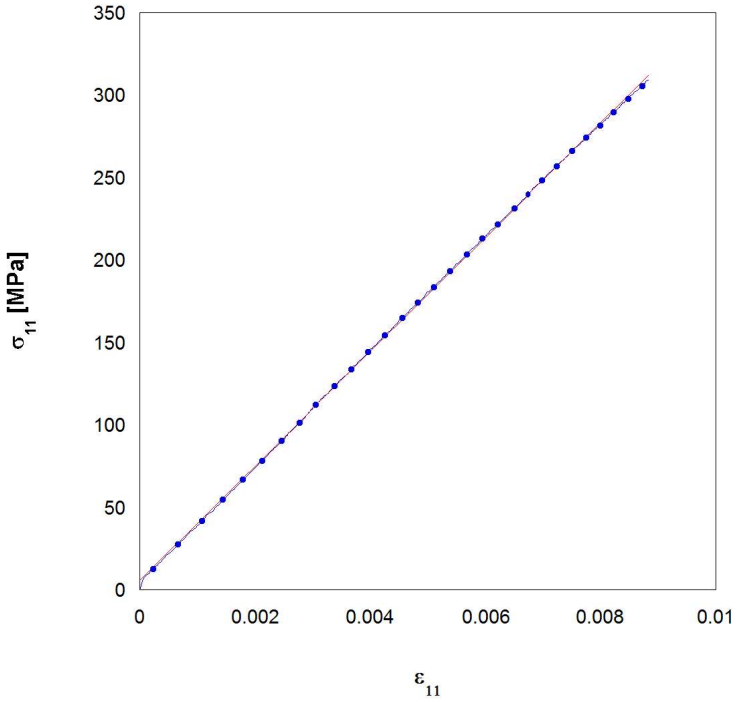
350
300
250
200
150
100
50
0
0
0.002
0.004
0.006
0.008
0.01
σ11 [MPa]
ε11

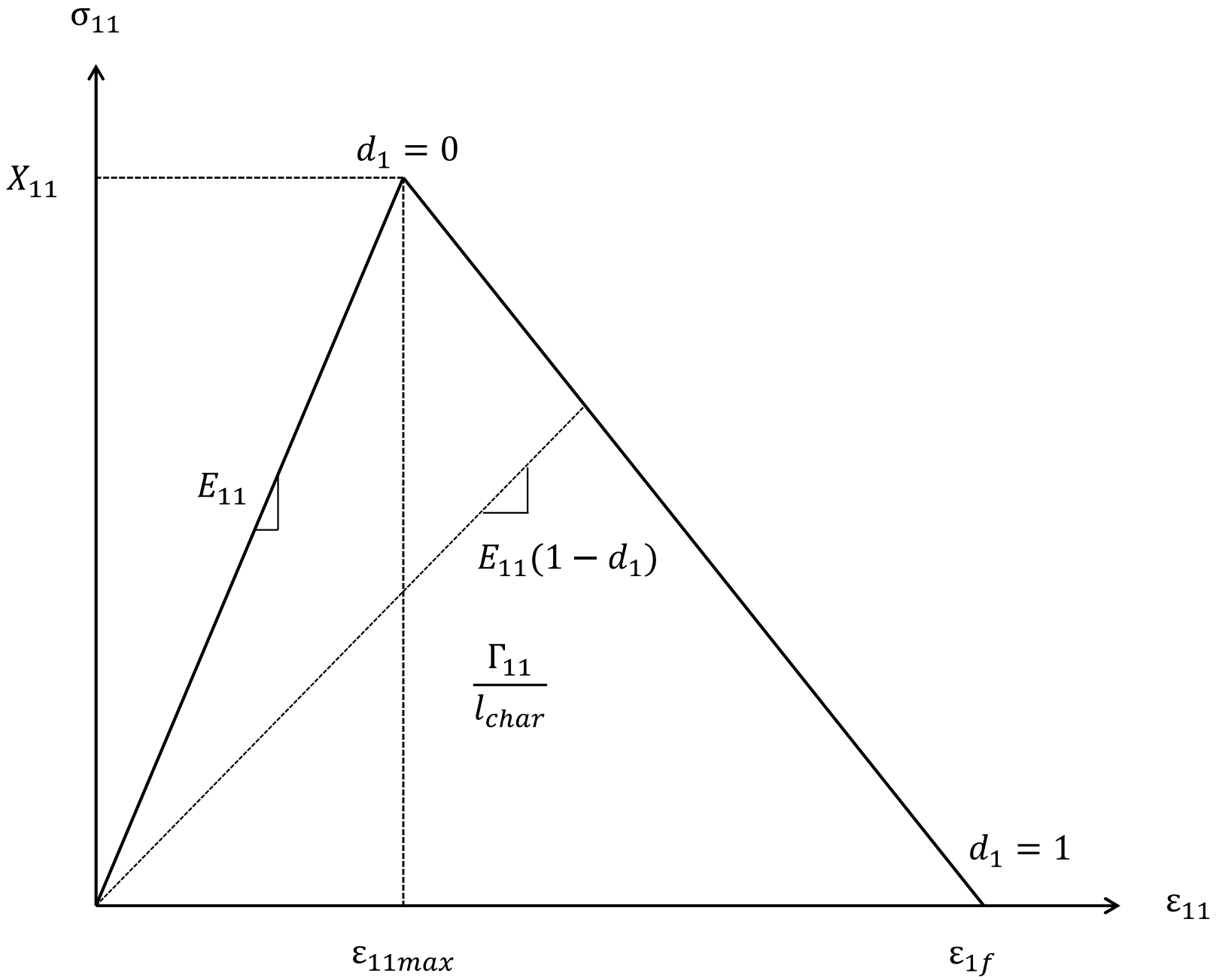
σ_{11}
X_{11}
$d_1 = 0$
E_{11}
$E_{11}(1 - d_1)$
$\frac{\Gamma_{11}}{l_{char}}$
$d_1 = 1$
ε_{11}
ε_{11max}
ε_{1f}

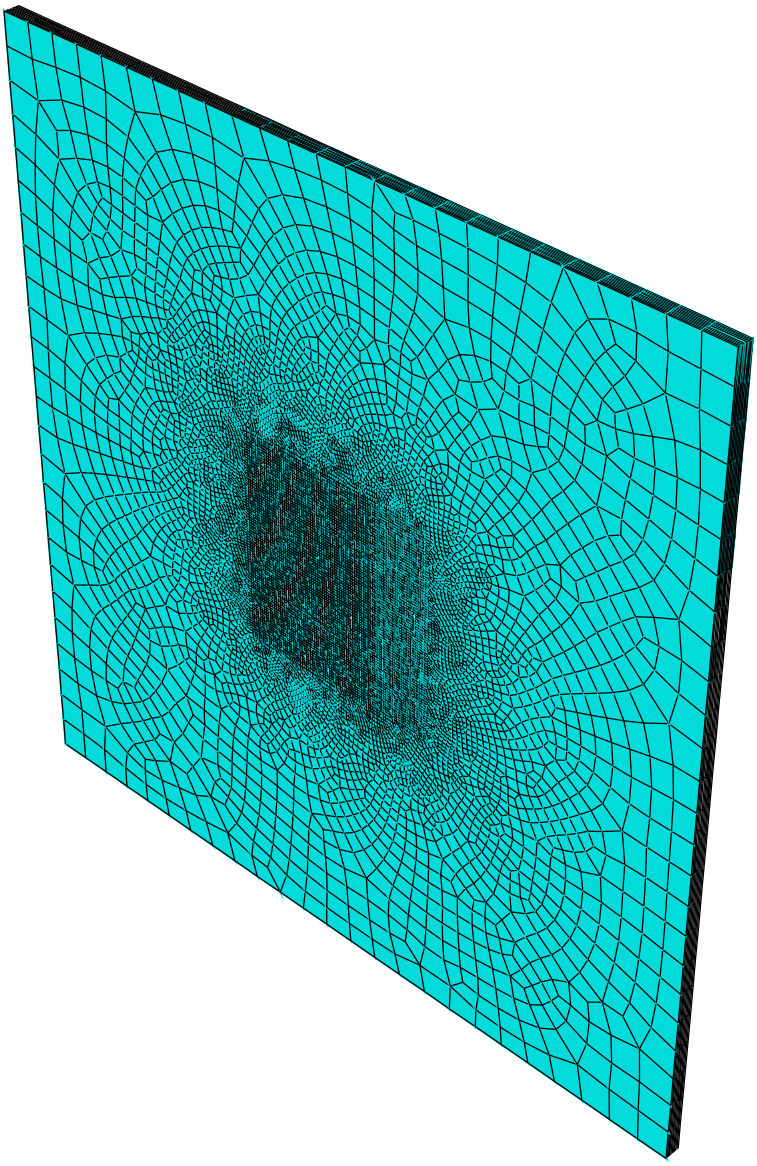

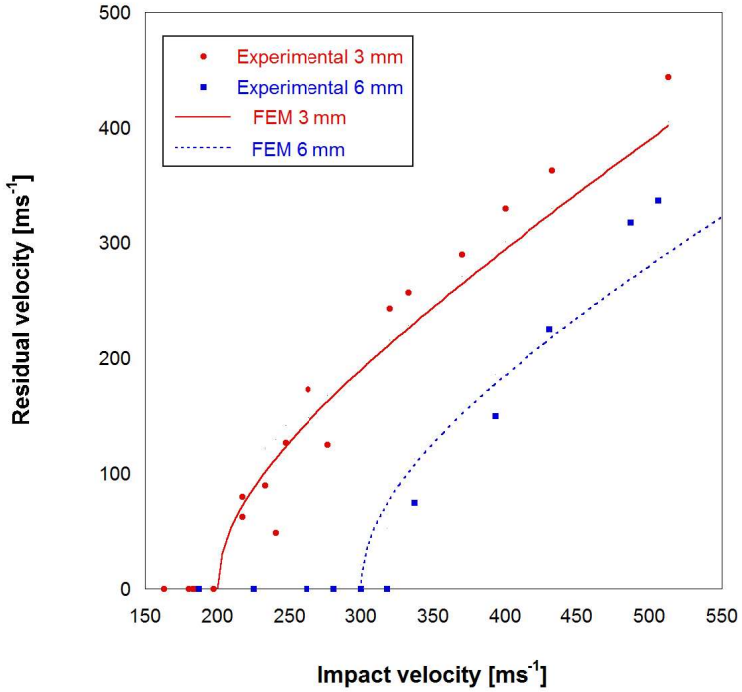
Experimental 3 mm
Experimental 6 mm
FEM 3 mm
FEM 6 mm
Residual velocity [ms-1]
Impact velocity [ms-1]
0
100
200
300
400
500
150
200
250
300
350
400
450
500
550

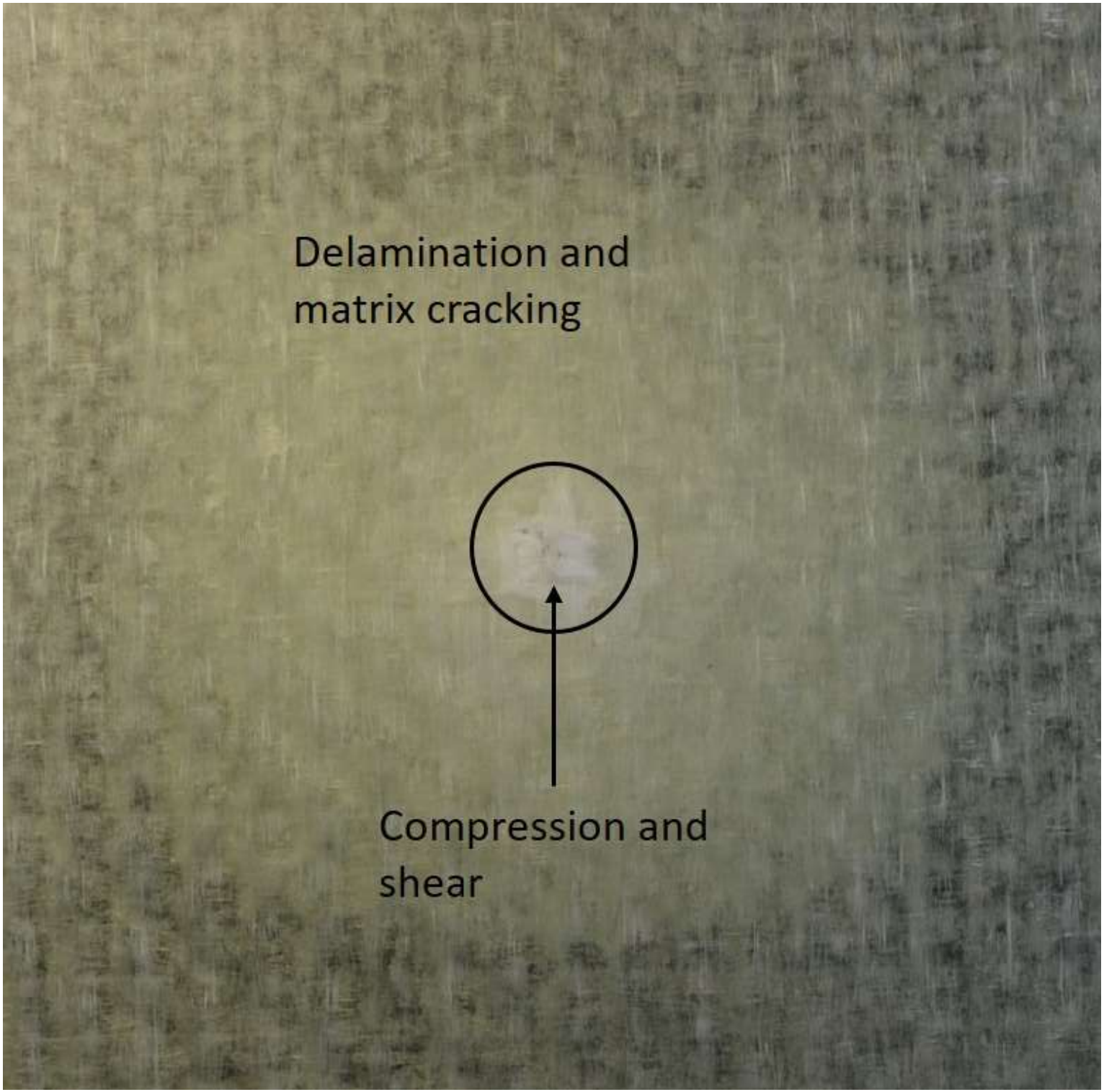
Delamination and
matrix cracking
Compression and
shear

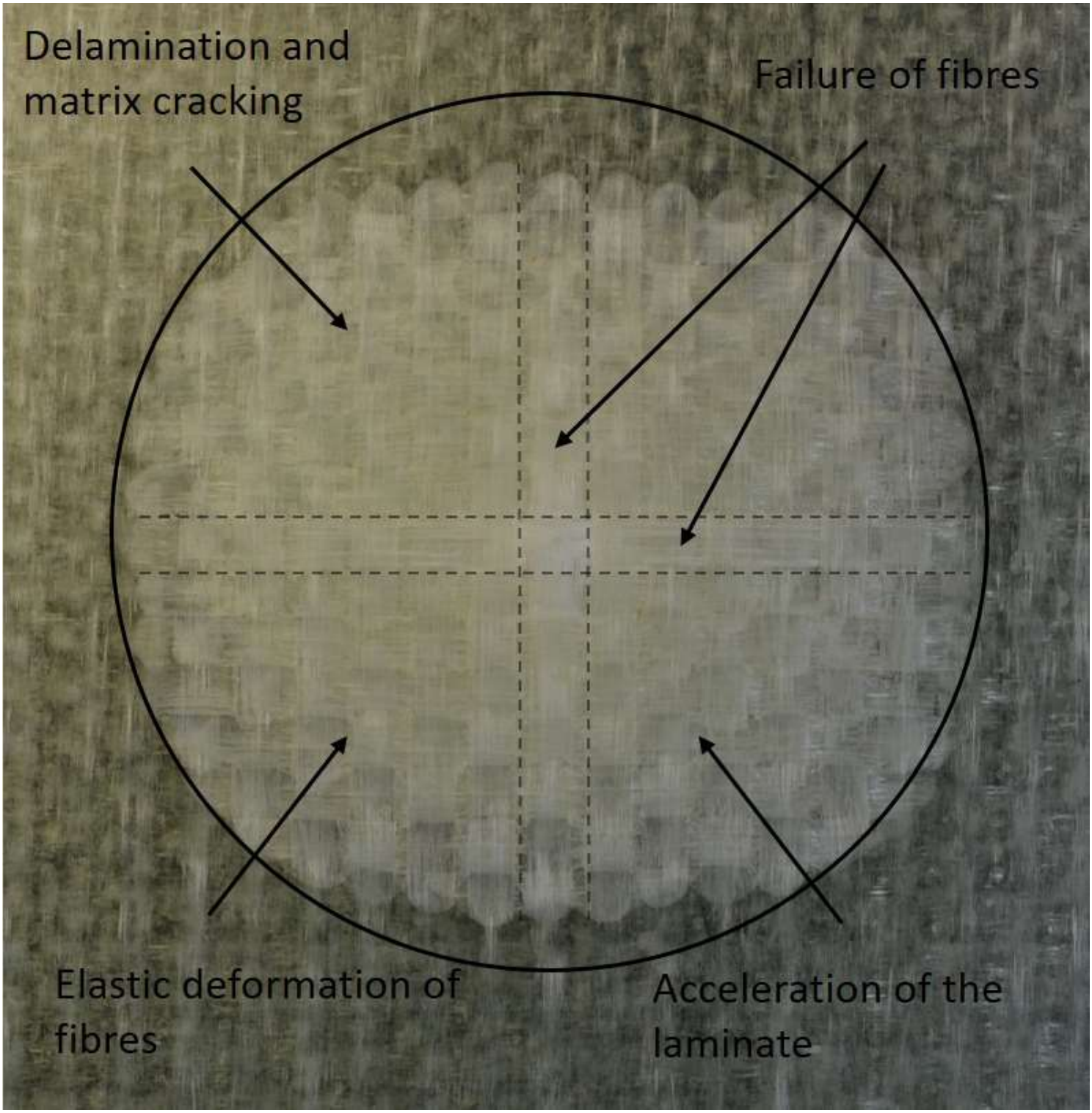
Delamination and matrix cracking
Failure of fibres
Elastic deformation of fibres
Acceleration of the laminate

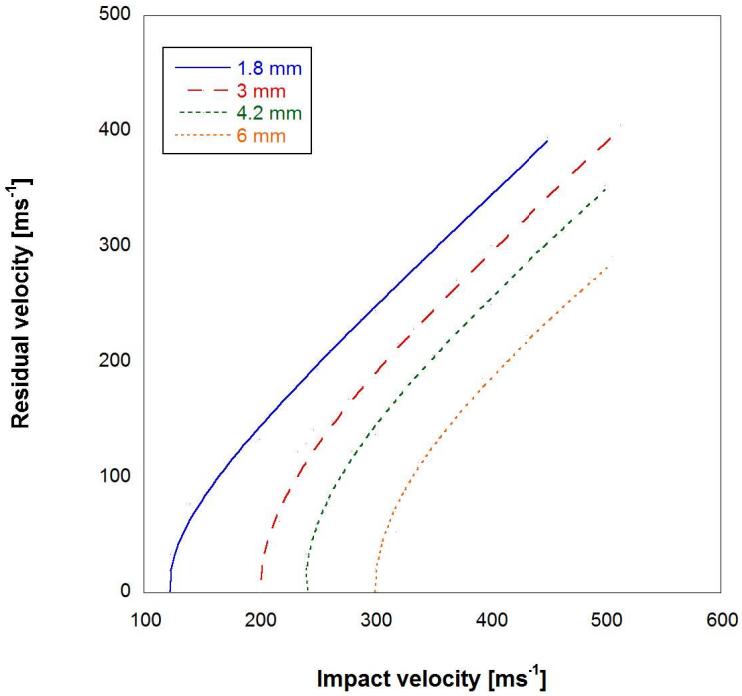
500
400
300
200
100
0
100
200
300
400
500
600
1.8 mm
3 mm
4.2 mm
6 mm
Residual velocity [ms-1]
Impact velocity [ms-1]

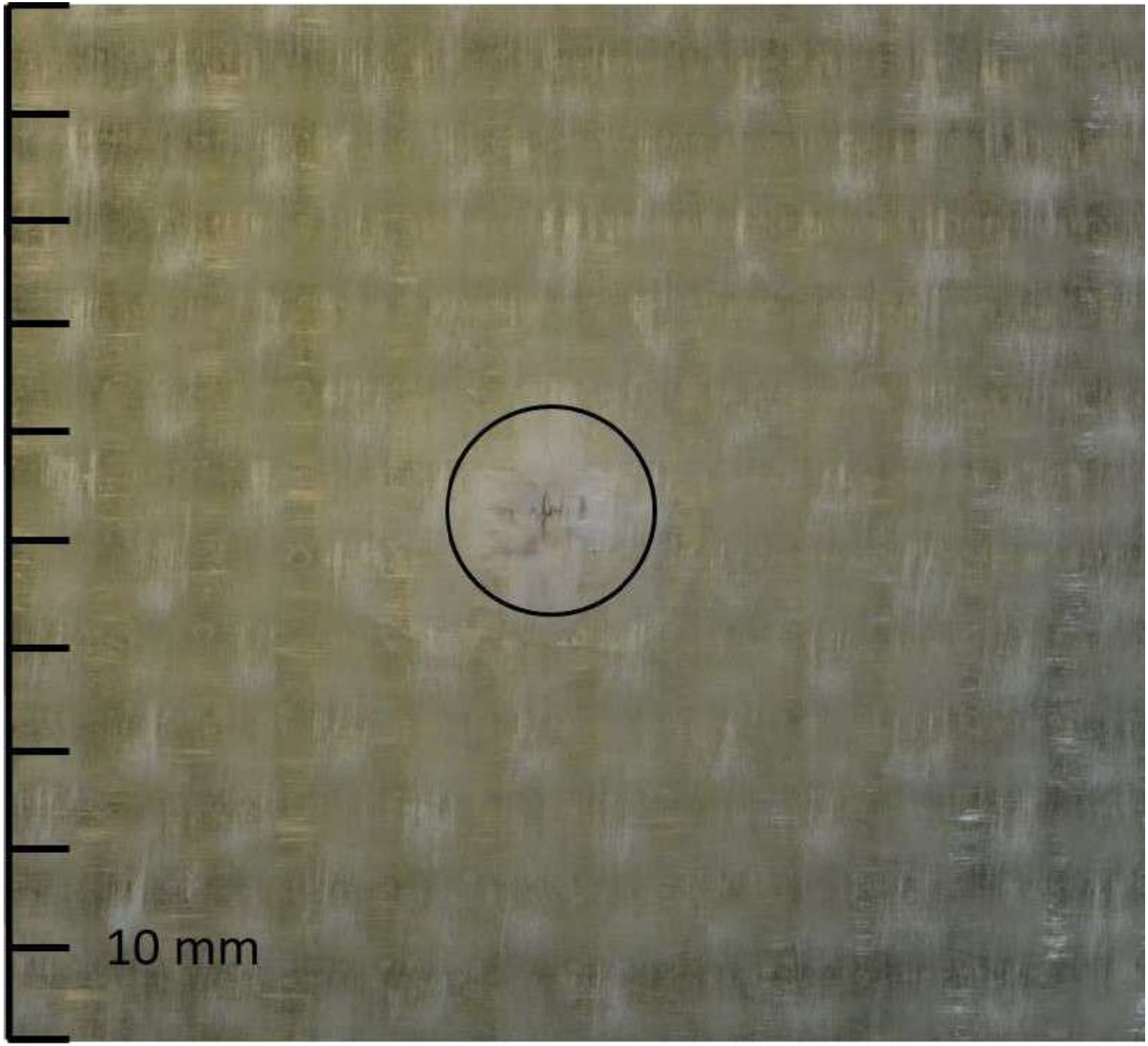
10 mm

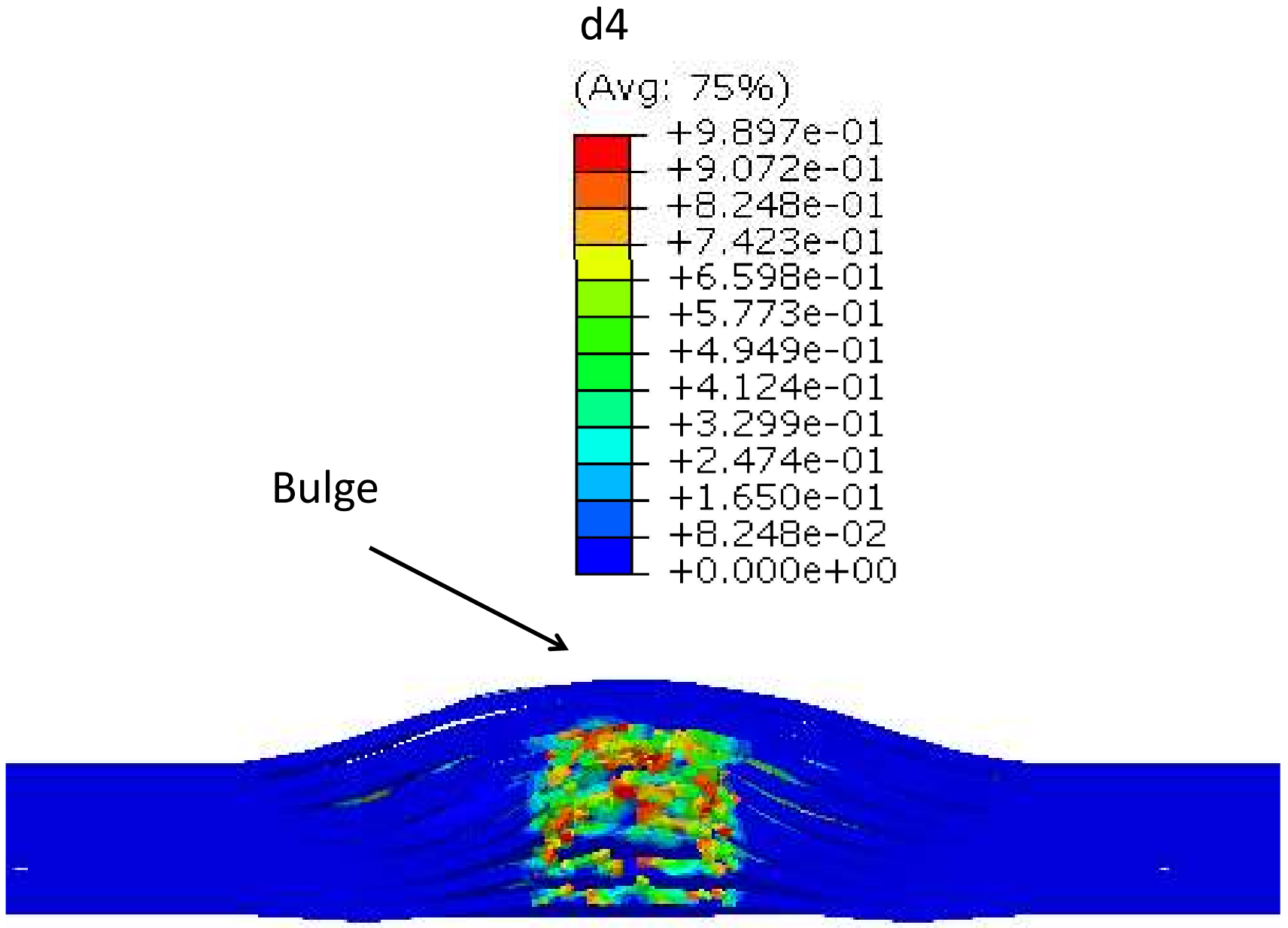
d4
(Avg: 75%)
+9.897e-01
+9.072e-01
+8.248e-01
+7.423e-01
+6.598e-01
+5.773e-01
+4.949e-01
+4.124e-01
+3.299e-01
+2.474e-01
+1.650e-01
+8.248e-02
+0.000e+00
Bulge

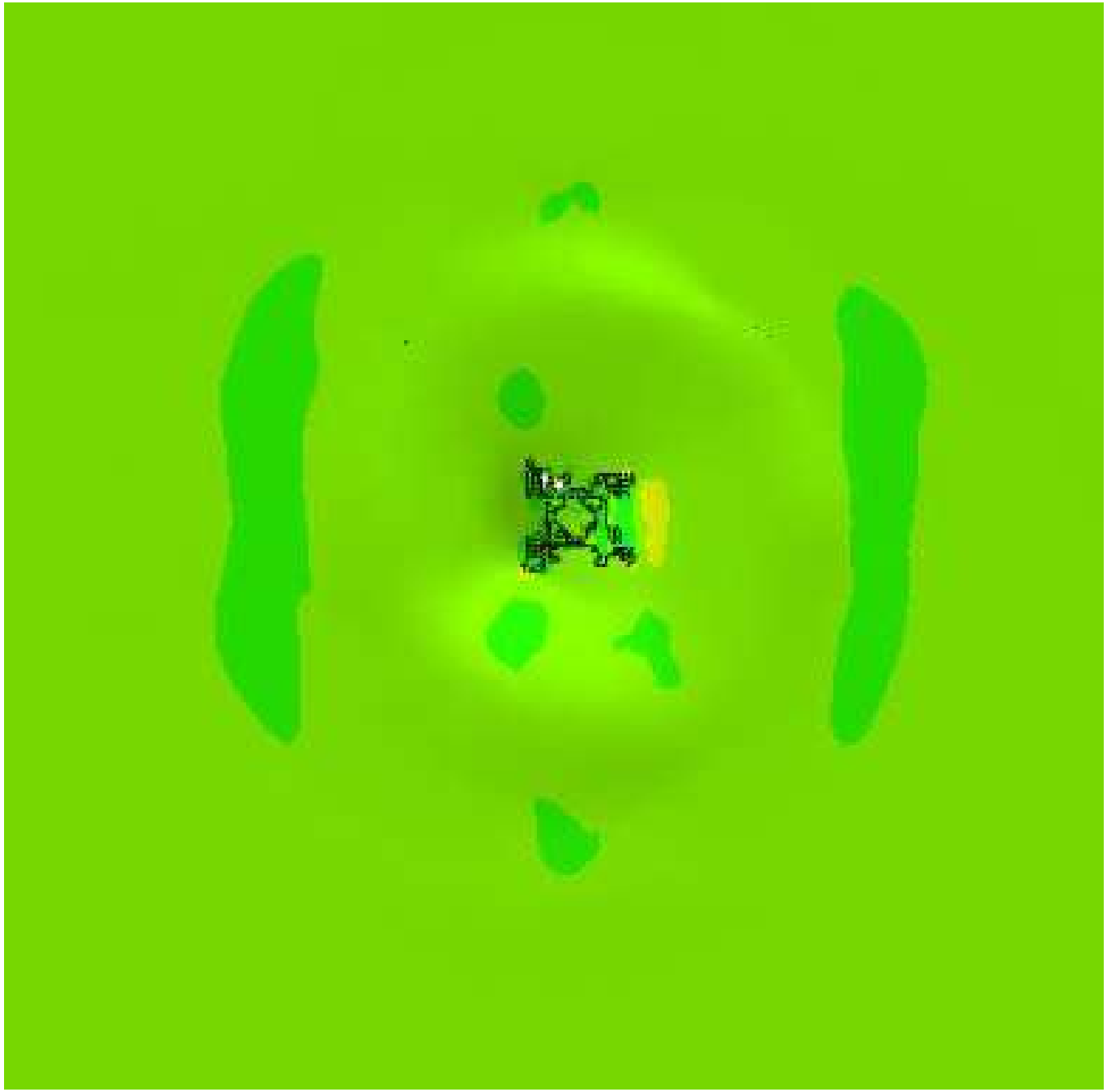
LE, LE11
(Avg: 75%)
+5.299e-02
+4.219e-02
+3.138e-02
+2.057e-02
+9.761e-03
-1.047e-03
-1.186e-02
-2.266e-02
-3.347e-02
-4.428e-02
-5.509e-02
-6.590e-02
-7.670e-02


LE, LE11
(Avg: 75%)
+5.299e-02
+4.219e-02
+3.138e-02
+2.057e-02
+9.761e-03
-1.047e-03
-1.186e-02
-2.266e-02
-3.347e-02
-4.428e-02
-5.509e-02
-6.590e-02
-7.670e-02


LE, LE22
(Avg: 75%)
+1.824e-01
+1.585e-01
+1.346e-01
+1.107e-01
+8.680e-02
+6.290e-02
+3.899e-02
+1.509e-02
-8.814e-03
-3.272e-02
-5.662e-02
-8.053e-02
-1.044e-01


LE, LE22
(Avg: 75%)
+1.824e-01
+1.585e-01
+1.346e-01
+1.107e-01
+8.680e-02
+6.290e-02
+3.899e-02
+1.509e-02
-8.814e-03
-3.272e-02
-5.662e-02
-8.053e-02
-1.044e-01

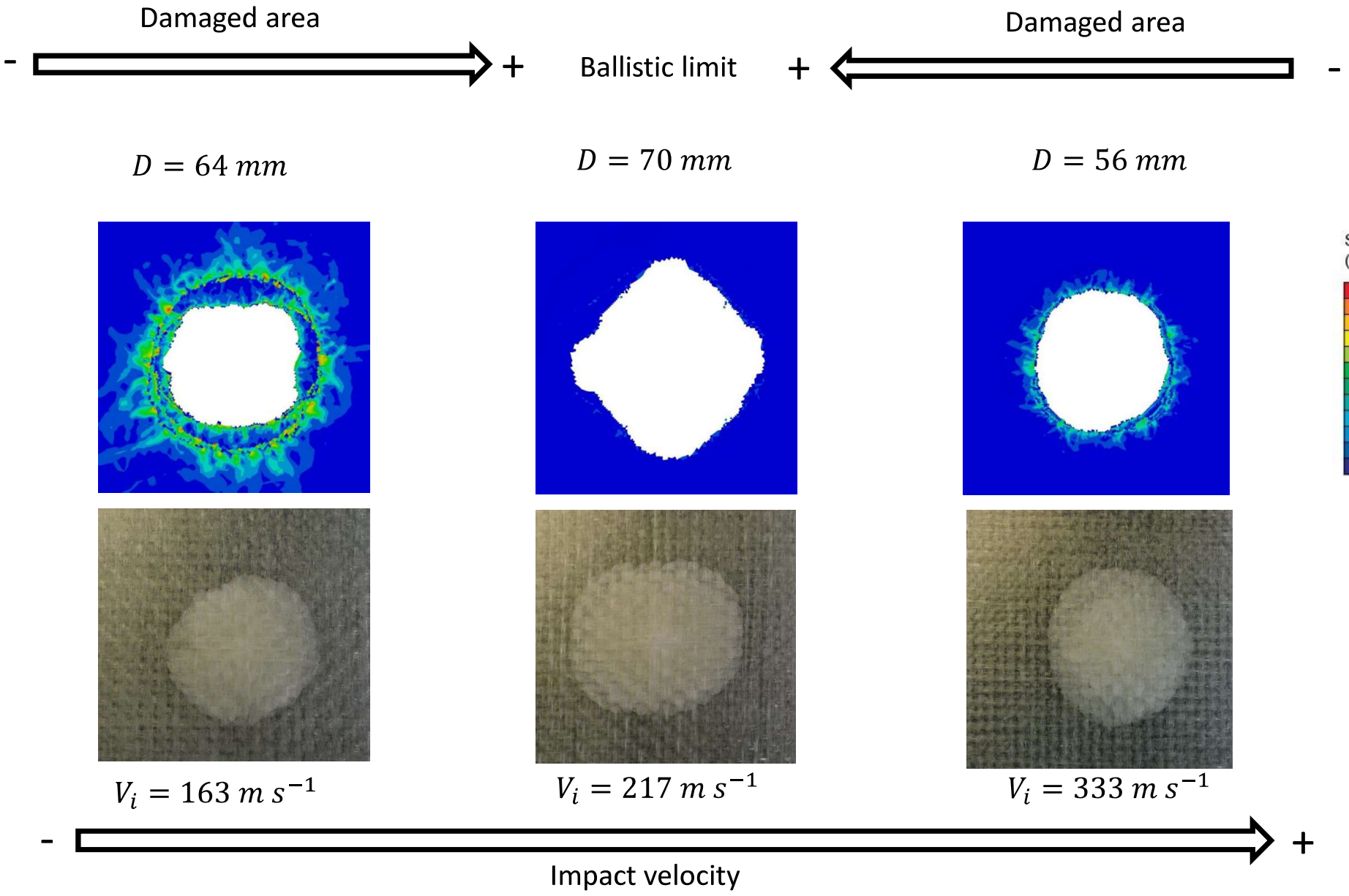
Damaged area
-
+
Ballistic limit
+
Damaged area
-
$D = 64\ mm$
$D = 70\ mm$
$D = 56\ mm$
SDEG
(Avg: 75%)
+1.000e+00
+9.167e-01
+8.333e-01
+7.500e-01
+6.667e-01
+5.833e-01
+5.000e-01
+4.167e-01
+3.333e-01
+2.500e-01
+1.667e-01
+8.333e-02
+0.000e+00
$V_i = 163\ m\ s^{-1}$
$V_i = 217\ m\ s^{-1}$
$V_i = 333\ m\ s^{-1}$
-
+
Impact velocity

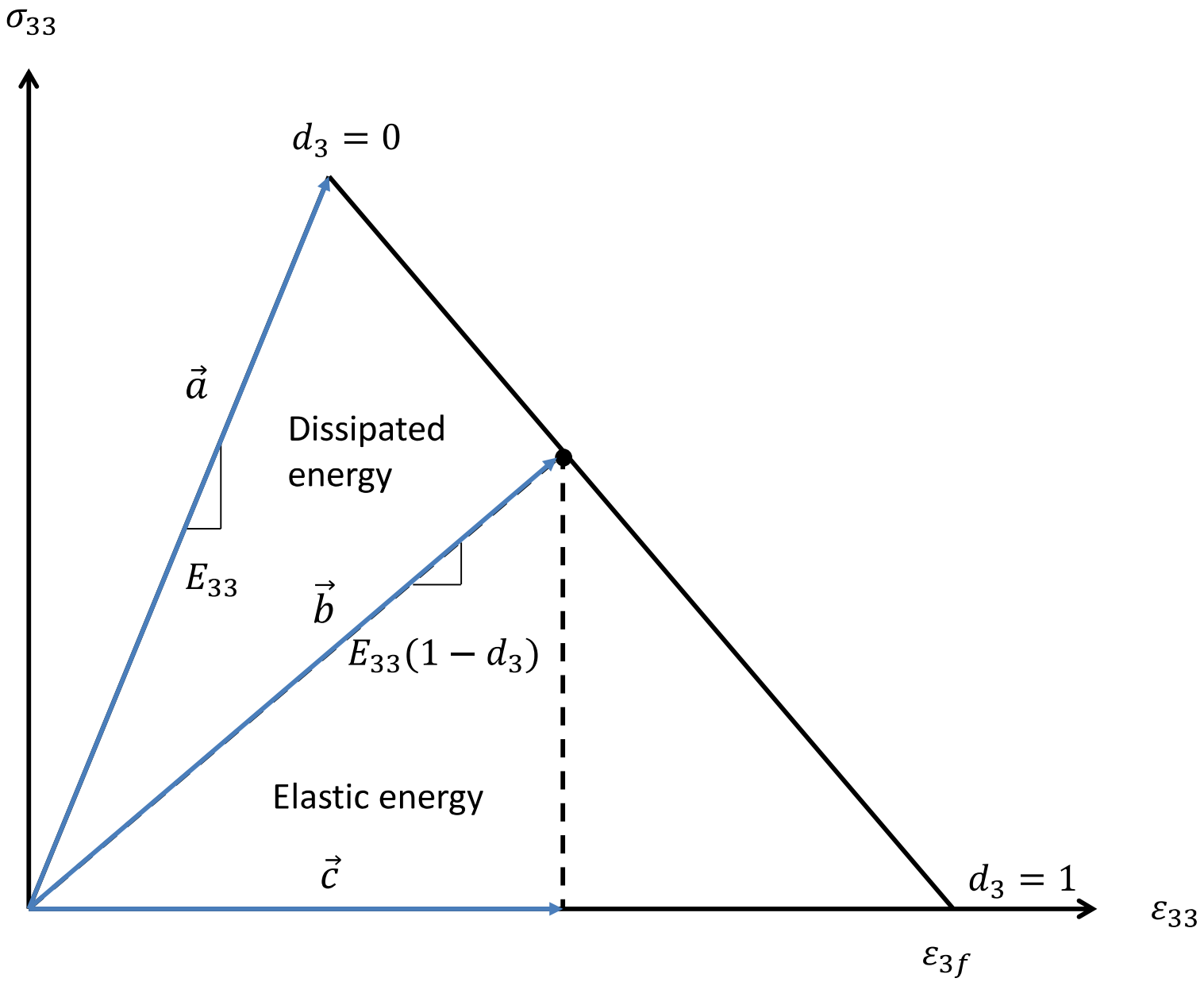
σ_{33}
$d_3 = 0$
$\vec{a}$
Dissipated energy
E_{33}
$\vec{b}$
$E_{33}(1 - d_3)$
Elastic energy
$\vec{c}$
$d_3 = 1$
ε_{33}
ε_{3f}

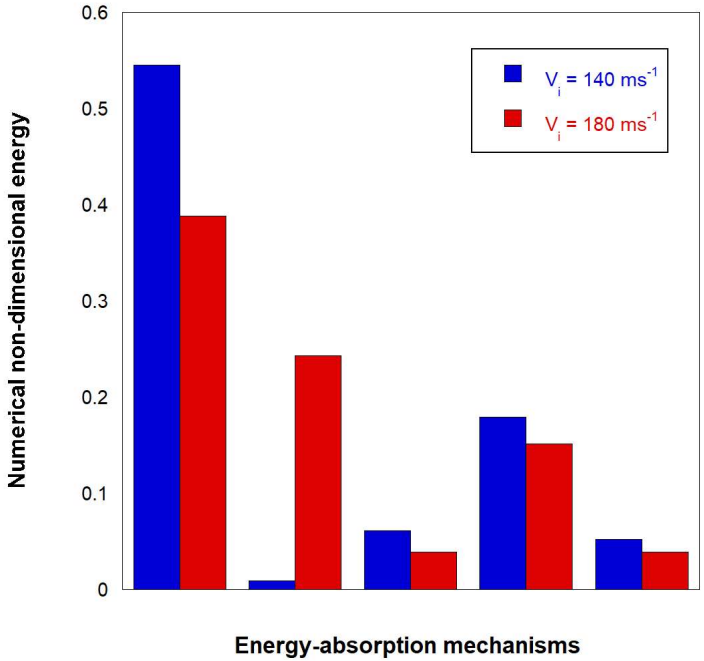
0.6
0.5
0.4
0.3
0.2
0.1
0
Numerical non-dimensional energy
V_i = 140 ms^{-1}
V_i = 180 ms^{-1}
Energy-absorption mechanisms

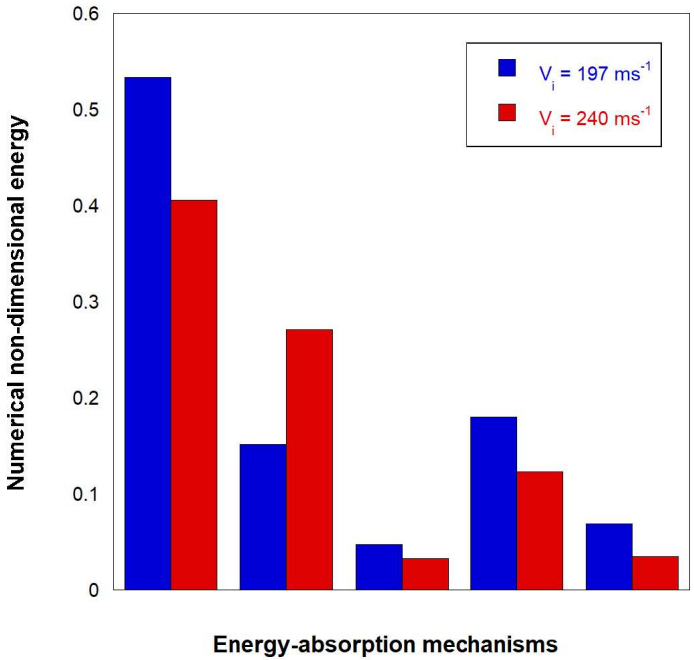
0.6
0.5
0.4
0.3
0.2
0.1
0
Numerical non-dimensional energy
V_i = 197 ms^-1
V_i = 240 ms^-1
Energy-absorption mechanisms

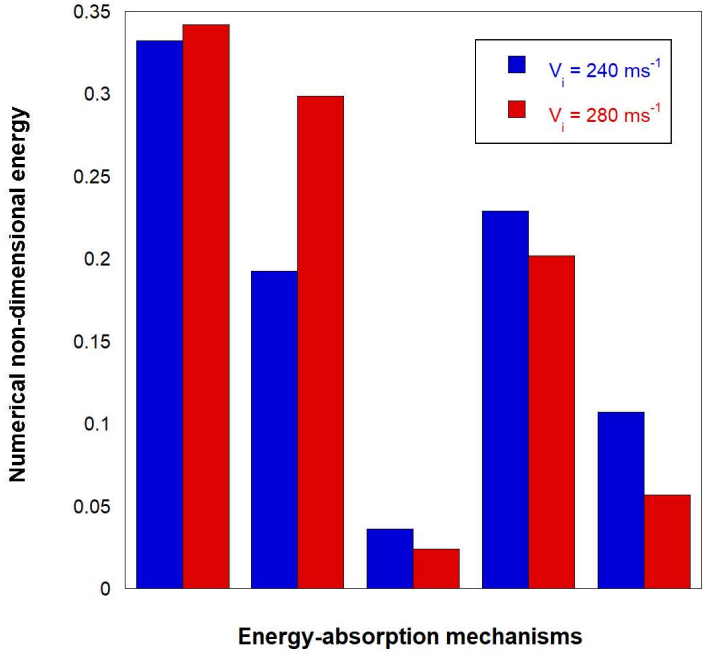
0.35
0.3
0.25
0.2
0.15
0.1
0.05
0
Numerical non-dimensional energy
V_i = 240 ms^-1
V_i = 280 ms^-1
Energy-absorption mechanisms

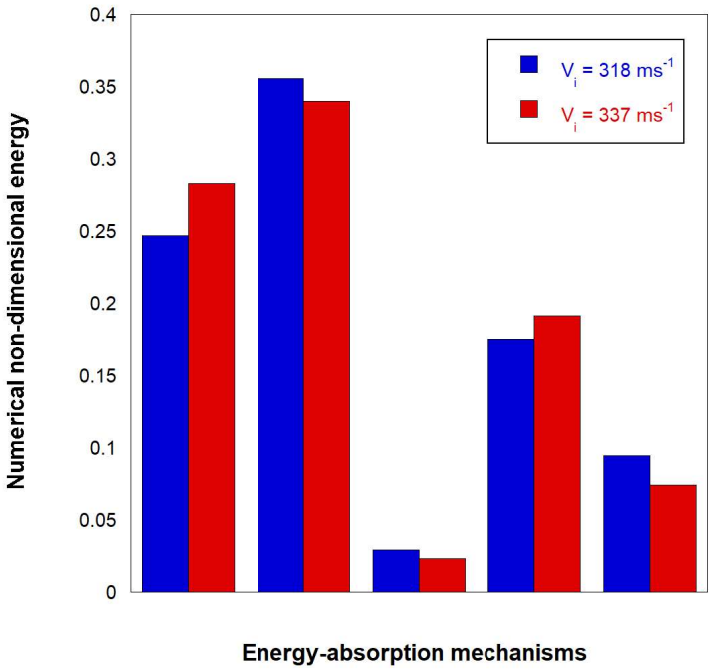
0.4
0.35
0.3
0.25
0.2
0.15
0.1
0.05
0
Numerical non-dimensional energy
V_i = 318 ms^-1
V_i = 337 ms^-1
Energy-absorption mechanisms

Conflict of interest

Declaration of Competing Interest
The authors declare that they have no known competing financial interests or personal relationships that could have appeared to influence the work reported in this paper.